FLORIDA INTERNATIONAL UNIVERSITY

Miami, Florida

NOVEL CONFORMAL STRONGLY COUPLED MAGNETIC RESONACE

SYSTEMS

A thesis submitted in partial fulfillment of

the requirements for the degree of

MASTER OF SCIENCE

in

ELECTRICAL ENGINEERING

by

Juan Barreto

2020

To: Dean John L. Volakis
      College of Engineering and Computing

This thesis, written by Juan Barreto, and entitled Novel Conformal Strongly Coupled Magnetic Resonance Systems, having been approved in respect to style and intellectual content, is referred to you for judgment.

We have read this thesis and recommend that it be approved.

_____
Nezih Pala

_____
Elias A. Alwan

_____
Stavros V. Georgakopoulos, Major Professor

Date of Defense: November 4, 2020

The thesis of Juan Barreto is approved.

_____
Dean John L. Volakis
College of Engineering and Computing

_____
Andrés G. Gil
Vice President for Research and Economic Development
and Dean of the University Graduate School

Florida International University, 2020

ii

DEDICATION

I dedicate my dissertation work to my family and friends. A special feeling of gratitude to my parents, brother and sister.

ACKNOWLEDGMENTS

ABSTRACT OF THE THESIS

NOVEL CONFORMAL STRONGLY COUPLED MAGNETIC RESONANCE

SYSTEMS

by

Juan Barreto

Florida International University, 2020

Miami, Florida

Professor Stavros V. Georgakopoulos, Major Professor

Wireless Power Transfer (WPT) is an emerging technology in today's society. Recently, many advancements to WPT systems have been implemented, such as, the introduction of the Strongly Coupled Magnetic Resonance (SCMR) and Conformal SCMR (CSCMR) methods. These methods allow WPT systems to operate at increased distances with smaller dimensional footprints. However, their range is still limited and needs to be expanded, and their footprint is sometimes large and needs to be miniaturized. Therefore, the goal of this research is to develop new designs and methodologies that can achieve the range extension and miniaturization of CSCMR systems.

Furthermore, many wireless devices are used today in the proximity of the human body (e.g., wearable and implantable applications). Therefore, WPT systems should be safe to use when placed on or inside the human body. To address this need, the secondary goal of this research is to study the effects of WPT systems when placed on or inside the human body.

TABLE OF CONTENTS

LIST OF TABLES

LIST OF FIGURES

CHAPTER I. INTRODUCTION

1.1)   Problem Statement

Wireless power transfer (WPT) has attracted significant attention as usage in our daily life is expected to grow significantly, with forecasts predicting that the Global Wireless Power Transmission Market will reach 12 Billion USD by the end of 2022 [3], with most of the market share being in North America. WPT technologies are very important as they eliminate wires and enable new applications where wires are not feasible or potentially dangerous. Recent technological advancements in wireless communications and RF devices has paved the way for many wireless power applications including but not limited to electric vehicle (EV) [4] [5] charging, implantable medical devices (IMD) [6], mobile devices [7], Unmanned Aerial Vehicles (UAVs) [8] [9], IoT sensor networks [10], and radio frequency identification (RFID) [11] [12].

Inductive Power Transfer (IPT) or inductive coupling is the traditional method of delivering power wirelessly, which was first explored by Nikola Tesla [13], and it has been used in medical devices since the 1960's. The inductive coupling method has dominated the WPT market share as it provides sufficient efficiencies in very short-range distances (distances between TX and RX resonators are within 3 cm), which is beneficial for applications in mobile devices and Implantable Medical Devices (IMDs). However, inductive coupling cannot provide high efficiencies in mid-range distances (i.e., distances that are equal or greater than the maximum dimensions of TX/RX resonators [14]). In 2006, researchers at the Massachusetts Institute of Technology showed that wireless power transfer with high efficiencies can be achieved in the mid-range using strongly coupled resonators [15]. These researchers introduced the Strongly Coupled Magnetic Resonance

(SCMR) method that shows great promise for next-generation WPT systems Therefore, the aim of this thesis is to further advance SCMR systems by: a) miniaturizing their footprint, b) extending their range, and c) developing designs that can safely operate on or inside the human body.

1.2)   Context and Motivation

An ideal WPT system will transfer power with no power losses occurring (i.e., 100% efficiency), at long ranges while maintaining physically small footprints for the TX and RX elements. In addition, WPT systems should be insensitive to misalignment and operate safely and efficiently on or inside the human body. Research and development of WPT systems has focused on developing designs that can meet these requirements. However, current WPT system still face many challenges. Therefore, this research aims to advance current WPT technologies to meet the demands of future applications, where chargeable, wearable and implantable devices will be extensively used.

Today, many devices require their batteries to be charged and often times this charging occurs via a connection to a wire. Digital devices, such as, smartphones, tablets, laptops, TV's and virtual home assistants, will surely continue to see more usage over the coming years. Consequently, if new WPT systems are developed with longer ranges, insensitivity to TX and RX misalignments and safe operation near humans, then multiple user devices can be simultaneously and ubiquitously charged. Furthermore, such systems would eliminate wires, which are inconvenient, take space and could potentially cause hazardous conditions (i.e., patients at hospital could trip on wired devices). Therefore, this thesis will focus on the development of long-range and misalignment insensitive WPT systems that are very important for many current and future applications.

2

In medical applications (e.g., implantable and wearable sensors), devices need to must be small. Therefore, WPT systems on printed circuit boards (PCBs) are well suited for such applications, as they are compact, cheap and easy to fabricate. However, when WPT systems are placed directly on metal surfaces or on PCBs that require ground planes for return currents, their Power Transfer Efficiency (PTE) diminishes. This occurs because the presence of metal surfaces near WPT systems detrimentally affects their magnetic fields that provide the coupling between TX and RX. Furthermore, traditional SCMR systems are large to implement in applications where space is limited. In this thesis, we aim to develop WPT SCMR systems that address both issues and develop compact WPT systems that can provide high efficiency near metal objects (including ground planes).

In biomedical applications, many devices are implantable or wearable and they are potentially lifesaving to their users. Devices, such as, deep brain neurostimulators, cochlear implants, gastric stimulators, cardiac defibrillators, insulin pumps, foot drop implants, pacemakers, etc., keep certain body parts from malfunctioning and inform users if any problems arise. However, most of these devices have a finite lifetime because of limited battery storage. Consequently, it is very inconvenient for users to replace such devices when batteries are depleted, because such replacements often require risky and costly surgeries. On the contrary, WPT systems can be used to charge batteries of medical devices thereby eliminating the risks of surgeries and replacements. Therefore, in this thesis, novel implantable and wearable SCMR systems are studied.

While implantable and wearable devices with WPT systems can be very beneficial, the electromagnetic field (EMF) absorption by human tissues can be detrimental to human health and also affect the performance of WPT systems. In fact, non-profit organizations

3

such as the International Committee of Non-Ionizing Radiation Protection (ICNIRP) have set standards to ensure RF devices are safe for their operation near the human body. Therefore, in this thesis, we will study the performance of WPT systems near the body and examine the specific absorption rate (SAR) at numerous body locations to ensure high efficiency power transfer is safely achieved.

1.3)   Thesis Outline

The thesis is organized as follows: Chapter 2 discusses the WPT systems used in current literature, the fundamentals of the IPT, and SCMR/CSCMR methods. Chapter 3 investigates numerous miniaturization techniques and implement them on a CSCMR system. In Chapter 4, range extension of CSCMR systems is achieved using novel planar relay resonators. In Chapter 5, CSCMR systems for implantable and wearable devices are studied and their performance is validated using state-of-the-art simulation software (i.e., Sim4Life), and measurements. Finally, conclusions are discussed in Chapter 6.

CHAPTER II. WIRELESS POWER TRANSFER BACKGROUND AND

FUNDEMENTALS

In this chapter, the various WPT methods will be discussed and the fundamentals of the SCMR method will be thoroughly examined. This section will review the existing literature to give the important theoretical concepts that will be used to give readers background information.

Inductive coupling Power Transfer (IPT) is the traditional method of delivering power via a wireless medium and has been the subject of numerous research and commercial projects [16]- [17] [18] [19] [20]. Therefore, the IPT method is a commonly used solution for short distance WPT systems, as they provide high efficiencies when the gap between TX and RX elements is small. Beyond mid-range distances, the efficiency of such systems significantly decreases to well below 50%, rendering them almost unusable for such scenarios. The second most referenced method of WPT that was recently discovered is known as the strongly coupled magnetic resonance (SCMR). SCMR uses 4 coils/loops instead of 2 coils/loops, allowing it to have optimal performance past mid-range distances. While SCMR is better than IPT beyond mid-range distances, the SCMR method is still relatively new, and improvements to this method still need to be done. Other WPT methods, such as, the Capacitive Coupling Power Transfer (CCPT) and Magneto-Inductive Wave (MIW) Power Transfer [21, 22] have been proposed but they have not yielded many promising results; therefore, they will not be discussed in this thesis.

All near-field WPT methods share similar theoretical foundation. Ampere's law and Faraday's law of induction describe why power transfer is possible and they will be described in what follows. Suppose a pair of not necessarily resonant coils are physically

placed near each other with an exciting current I_1 flowing through coil one with N_1 number of turns, as shown in Figure 2.3 [23]. If I_1 is a time varying current, an induced EMF will be generated in the second coil due to the change in magnetic flux. The induced EMF is given by Equation (2.1) as:

$$\varepsilon_{21} = -N_1 \frac{d\Phi}{dt} = \frac{-d}{dt} \iint\limits_{coil\ 1} \vec{B}_1 \cdot d\vec{A}_2 \tag{2.1}$$
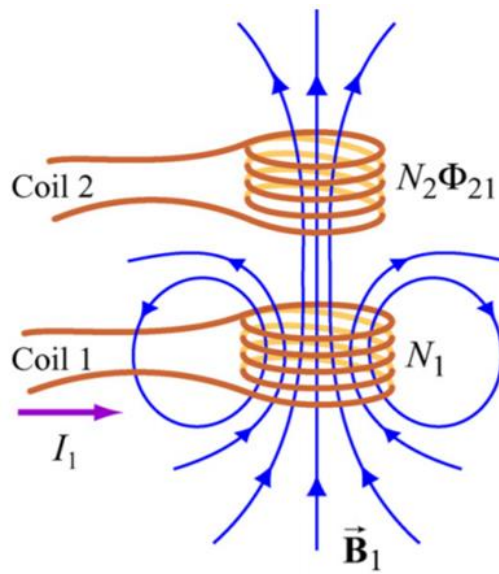
Figure 2.3. Coil one generating an EMF on coil two [23]

This produces a current flowing through coil two. The rate of change of magnetic flux going through coil two is proportional to the rate of change of the current in coil one, as given by Equation (2.2):

$$N_2 \frac{d\Phi_{21}}{dt} = M_{21} \frac{dI_1}{dt} \tag{2.2}$$

Therefore, the mutual inductance is rewritten as:

$$M_{21} = \frac{N_2 \Phi_{21}}{I_1} \tag{2.3}$$

The mutual inductance due to an exciting current in coil one and corresponding magnetic flux going through coil two is a function of the number of turns, the magnetic flux and exciting current as seen in Equation (2.3). A similar analysis may be done, where an exciting current in coil two generates a magnetic flux that goes through coil one to produce a mutually induced link M_{12} given by Equation (2.4) below:

$$M_{12} = \frac{N_1 \Phi_{12}}{I_2} \tag{2.4}$$

Due to the reciprocity theorem which combines Ampere's and Biot-Savart's law, the mutual inductance constants can be shown to be equal as seen in Equation (2.5) below:

$$M_{12} = M_{21} = M \tag{2.5}$$

The analysis done above, shows that mutual inductance is simply the ratio of the magnetic flux going through the number of turns in one coil and the exciting current in the opposite coil that generates the magnetic field. Therefore, mutual inductance can be thought of as the effect that one coil has on the other based on the current changing on one coil. Also, the coupling coefficient can be written as

$$\kappa_{12} = \frac{M_{12}}{\sqrt{L_1 L_2}} = \frac{N_1 \Phi_{12}}{I_2 \sqrt{L_1 L_2}} \tag{2.6}$$

This concept is fundamental to near-field inductive power transfer and describes how it is possible to transfer power over a magnetic field.

2.1)   Inductive Power Transfer

Inductive coupling via two resonant coils is the traditional and (as of the time of writing this thesis) the most widely used method of WPT and is commonly known as the Inductive Power Transfer (IPT) method. Its popularity stems from its simplicity and high efficiency in short distances and its relatively low operating frequencies. Specifically, the transmitter (TX) and receiver (RX) are composed of a coil with parasitic inductance and capacitance that determine the WPT system's operating frequency. A complete IPT system is shown in Figure 4.2. It begins with a DC voltage supply that feeds the transmitter with power. An oscillator and power amplifier are used to convert the DC signal to the high frequency that is determined by the resonant frequency of the coils. Then, a capacitor in series or parallel is required to compensate the inductance of the IPT system and provide optimal efficiency. The TX element transmits the power to RX element wirelessly. A rectifier is used to convert the high frequency signal received by the RX to a DC signal and deliver it to a load.
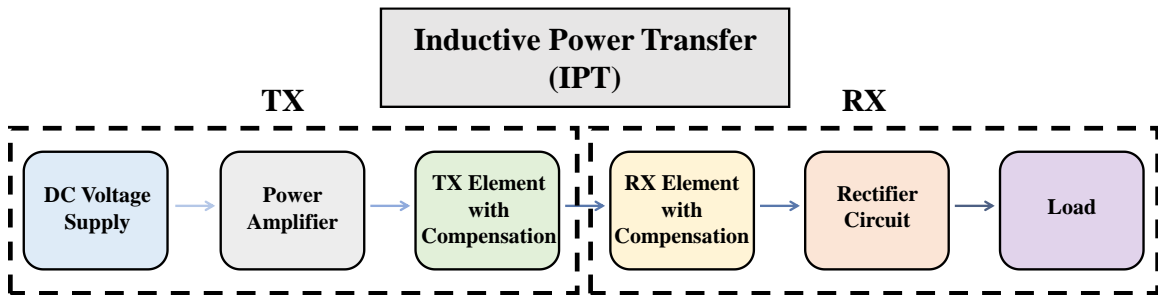
Figure 4.2. Inductive Power Transfer System

High efficiency is desired at every stage of the WPT system. Therefore, significant research has been done to optimize the efficiency of the different stages of WPT systems and provide the best possible performance. For instance, high efficiency and high-power class E amplifiers are of great interest and have been thoroughly studied. Furthermore,

8

compensation topologies at the TX and RX circuit stages have been investigated. Compensation is particularly important for IPT methods because coils are typically loosely coupled, and the coupling coefficient is significantly less than 1. When this is the case, the power transmitted to the load can be approximated by Equation (2.7)

$$P_{L,\kappa<<1} \approx \frac{L_2}{L_1}|V_1|^2 \frac{R_L}{(\omega L_2 + X_L)^2 + R_L^2}\kappa_{12}^2 \tag{2.7}$$

The above equation demonstrates why a compensation network is necessary for IPT systems. Both primary and secondary circuits require a capacitive element to eliminate the imaginary part. We can see that by reducing the $(\omega L_2 + X_L)^2$ term, then the power delivered to the load may improve significantly and thereby increasing the system's efficiency. Figure 2.5 demonstrates how this compensation can be realized for IPT systems [24].
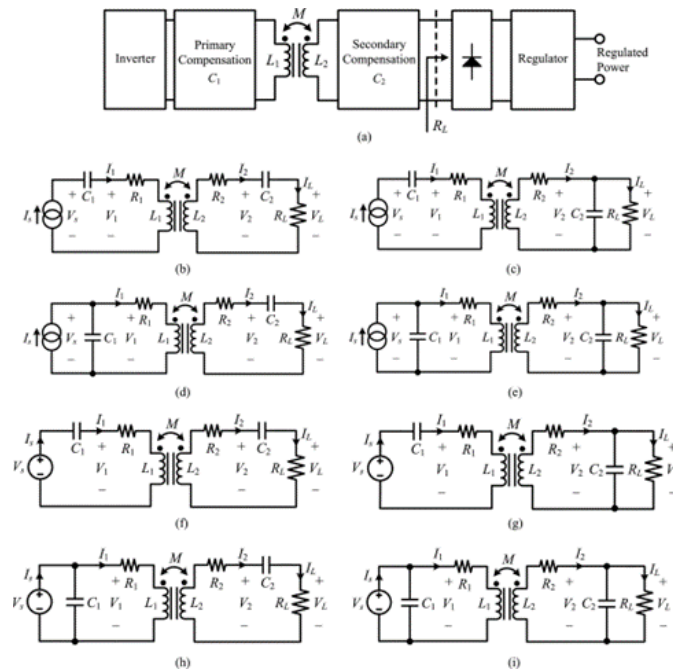
Figure 2.5. Compensation network topologies: ISS, ISP, IPS, IPP, VSS, VSP, VPS, VPP [24]

There is a possibility of eight different combinations. The network can either be a voltage

source or current source with the primary and secondary compensation either being a capacitor in series or parallel. The eight possible combinations are the following eight topologies: ISS, ISP, IPS, IPP, VSS, VSP, VPS, VPP. These different topologies offer certain advantages and disadvantages. However, as was seen in [24], the following characteristics are important to account for, when choosing the topology of the compensation; namely, the frequency of maximum efficiency, maximum load power transfer, load-independent output voltage or current, coupling coefficient independent compensation and allowance of no magnetic coupling (meaning that nothing will burn due to a short circuit). A comparative study of the eight topologies was completed and the resulting conclusions found that the current source SS and SP topologies generally satisfied the five characteristics successfully.

It is a well-known fact that the IPT method offers great efficiency at small distances, but its efficiency diminishes at larger distances. While the fundamental principles between the IPT and SCMR method are the same (i.e., both methods use Ampere's and Faraday's laws), they differ in one key manner that distinguishes them. SCMR uses four loops/coils (a source, a load, a TX and an RX resonator loop/coil), whereas IPT uses just two. The decoupling of the source/load loops from the TX/RX resonators, enables the system to use resonators that have very high Q-factors. Also, the SCMR method chooses the capacitors connected to the TX/RX resonators so that they operate at the frequency where the loops/coils exhibit their highest Q-factor. For these reasons, SCMR systems can provide significantly higher efficiency at long distances than conventional IPT systems; therefore, the SCMR method was chosen in this thesis.

2.2)   Strongly Coupled Magnetic Resonance

To understand why Strongly Coupled Magnetic Resonance (SCMR) systems are able to perform with great efficiency in the mid-range, circuit theory analysis will be done. In Figure 2.6 [25], the standard SCMR schematic is drawn, it is composed of four main components including: 1) a source loop where an alternating current is feed into, 2) a TX resonant loop or coil to transmit power wirelessly, 3) a RX resonant loop or coil to receive the transmitted power wirelessly, and 4) a load loop where the power is delivered to. As previously mentioned, the premise of this transfer begins with Faradays law of induction, this occurs when the source loop is excited by an AC current, which produces a magnetic field that in turn induces a voltage on the RX coil or loop due to the change in magnetic flux. The same process occurs throughout each loop or coil until the power is finally delivered to the load loop.
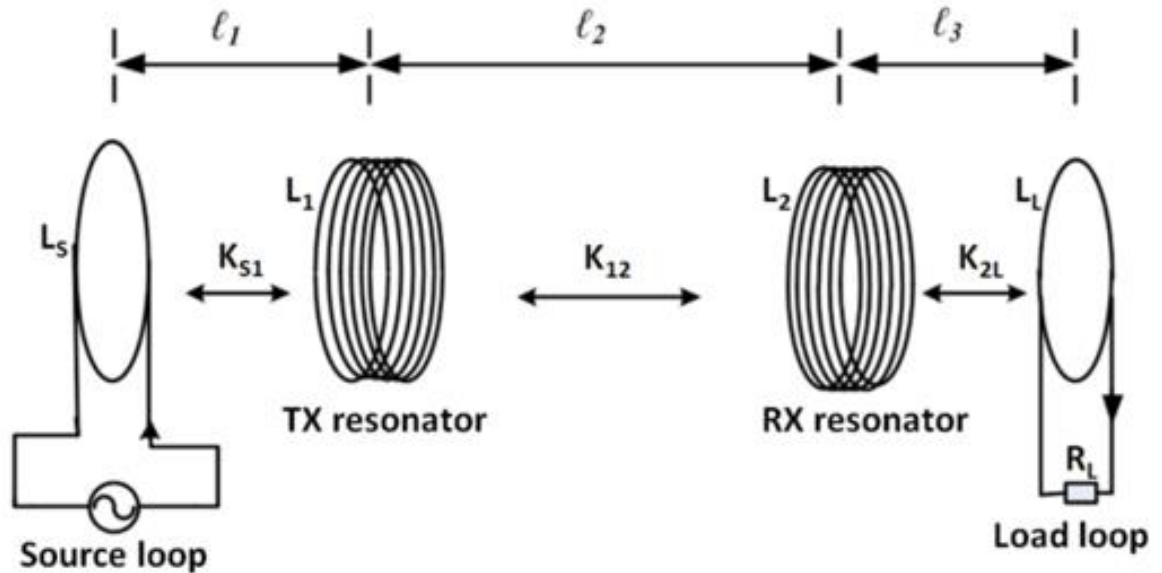
Figure 2.6. Schematic of a standard SCMR system *[25]*

Figure 2.7 shows the equivalent circuit, where R_s and V_s are the internal source resistance and voltage, respectively. The source and load loop resistances and inductances are R_S and

11

L_1, and R_L, L_4 respectively. RX and TX resonators have a capacitance, inductance, and resistance of R_2, L_2, C_2, and R_3, L_3, C_3 respectively. The coupling coefficient between source and TX resonator is denoted as κ_{S1}, between TX and RX resonators as κ_{12}, and between RX resonator and load loop as κ_{2L}. Coupling terms between loops or coils not directly facing each other can be ignored as their values are negligible. The coupling between the resonators increases the overall mutual inductance between the TX and RX elements of the WPT system thereby allowing SCMR and CSCMR systems to work at extended ranges as compared to traditional IPT methods.
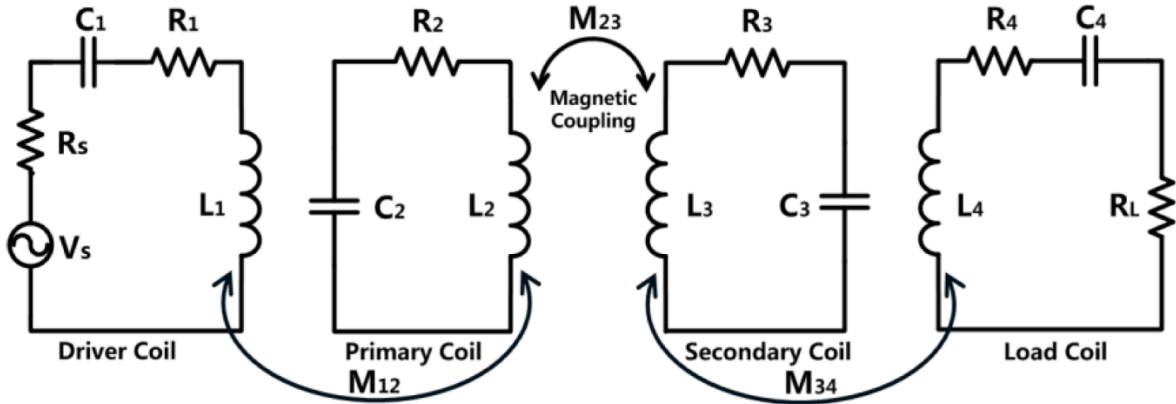
Figure 2.7. Equivalent circuit of standard SCMR system [1]

Looking closer at the equivalent circuits of the TX/RX resonators, it can be seen that they are simply composed of a resistance, inductance and capacitance, which form resonant circuits. To achieve highly efficient SCMR systems, the TX and RX must operate at the same frequency and this operating frequency must coincide with the frequency where the Q-factors of the RX and TX resonator loops are naturally maximum. The Q-factor represents how well the resonators are able to store energy. In fact, the Q-factor is proportional to the ratio of the energy stored (reactance) to the energy dissipated (resistance) during each cycle of oscillation. Therefore, high Q-factors mean that high

amounts of energy are able to be stored within reactive components while maintaining minimal losses per cycle. This is shown clearly in Equation (2.9), where it is seen that by decreasing losses due to resistance in the system will allow for high Q-factors to be achieved. The energy in a resonant circuit oscillates between the inductor and the capacitor at the resonant frequency. Also, the energy is dissipated in the circuit's resistance, R, and the magnitudes of the circuit's inductive and capacitive reactance should be equal under resonant conditions. Therefore, $\omega L = \frac{1}{\omega C}$ and the resonant frequency can be calculated as:

$$\omega_0 = \frac{1}{\sqrt{LC}} \tag{2.8}$$

where $\omega_0 = 2\pi f_r$, and the Q-factor can be written as [26]:

$$Q = \frac{\omega_r L}{R} = \frac{2\pi f_r L}{R} \tag{2.9}$$

If the resonator is a resonant helix, then the Q-factor may be written as [23]:

$$Q = \frac{2\pi f_r L_{helix}}{R_{ohm} + R_{rad}} \tag{2.10}$$

where L_{helix}, R_{rad}, and R_{ohm} are the self-inductance, radiation resistance, and ohmic resistance of the short helix or solenoid ($2r > h$) and are determined mathematically by Equation (2.11), Equation (2.12), Equation (2.13) [27] - [28] [29] [30]:

$$L_{helix} = \mu_0 r N^2 \left[ln\left(\frac{8r}{r_c}\right) - 2 \right] \tag{2.11}$$

$$R_{rad} = \left(\frac{\pi}{6}\right) \eta_0 N^2 \left(\frac{2\pi f_r}{c}\right)^4 \tag{2.12}$$

$$R_{ohm(helix)} = \left(\sqrt{\mu_0 \rho \pi f_r}\right) \frac{Nr}{r_c} \tag{2.13}$$

The efficiency of a traditional SCMR system with both resonators operating at the same

resonant frequency f_r can be written as follows according to [31]:

$$\eta(f_r) = \frac{\kappa^2_{(TX_{RX})}(f_r)Q_{TX}(f_r)Q_{RX(f_r)}}{1 + \kappa^2_{(TX_{RX})}(f_r)Q_{TX}(f_r)Q_{RX(f_r)}} \tag{2.14}$$

Equation (2.14) highlights the importance of having high Q-factors, since high Q-factors can provide great efficiencies even when the mutual coupling $\kappa^2_{(TX_{RX})}$ between resonators are not as high. In fact, this is the reason why SCMR provides higher efficiencies at greater distances. Assuming the TX and RX resonators are identical, $Q_{TX} = Q_{RX}$ and Equation (2.14) may be rewritten as:

$$\eta(f_r) = \frac{\kappa^2_{(TX_{RX})}(f_r)Q^2_{TX}(f_r)}{1 + \kappa^2_{(TX_{RX})}(f_r)Q^2_{TX}(f_r)} \tag{2.15}$$

Therefore, Equation (2.15) may be used to calculate the efficiency between two strongly coupled magnetically resonant coils.

The limiting factor of the coupling coefficient is the magnetic flux. When the two coils are physically placed near each other, the coupling coefficient will always be highest since this is when the most flux generated by the transmitting coil is coupled to the receiving coil. The coupling coefficient ranges from values of zero to one, one meaning that all of the magnetic flux generated by the transmitting coil is going through the receiving coil, and zero meaning that none of the magnetic flux generated by the transmitting coil is going through the receiving coil. When the coils are placed further apart, less flux goes through the receiving coil and the coupling coefficient decreases. This is the fundamental reason that causes the efficiency of WPT to decrease as the distance between the TX and RX elements increases.

To further investigate the effects of both the coupling coefficient and the quality factor, the transfer efficiency for a WPT system is plotted as a function of the coupling

14

coefficient and quality factor. Notably, the coupling coefficient of SCMR systems at mid-range distances is typically very small, since the coupling coefficient drops very fast as the distance between two coils increases. In most cases, the value of the coupling coefficient is going to reside under 0.1 leaving the system in the loosely coupled regime. To account for a loosely coupled WPT system, the quality factor must be increased to compensate. Figure 2.8 plots the WPT efficiency versus the quality factor of the TX/RX resonators for different coupling coefficients.
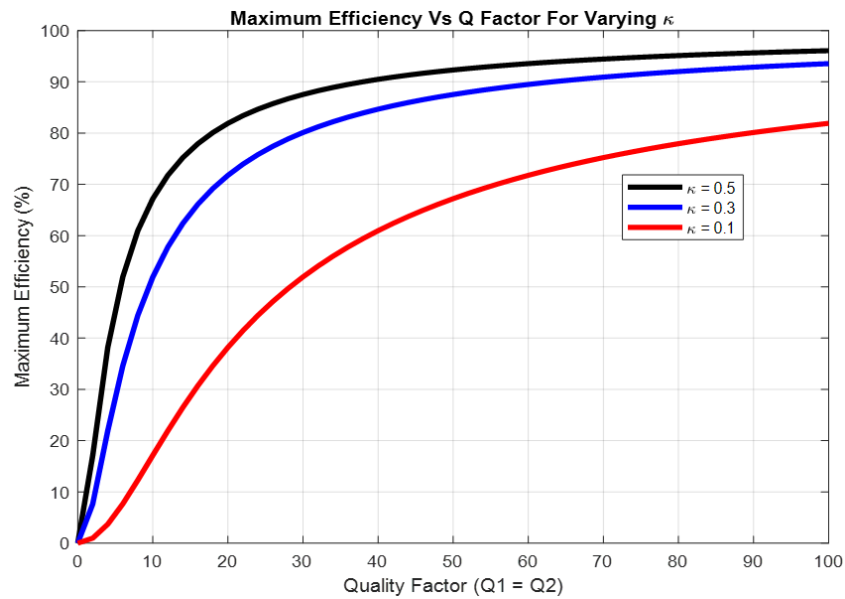
Figure 2.8. Maximum efficiency vs varying values of Q & κ

Specifically, three different values of the coupling coefficient were considered, namely, 0.1, 0.3 and 0.5. The following two conclusions can be drawn based on Figure 2.6: 1) the WPT efficiency increases as the coupling coefficient increases, which can be by decreasing the distance between the WPT TX and RX coils, and 2) the WPT efficiency increases as the quality factor increases. These two conclusions prove the fundamental operation of SCMR systems that achieve high WPT efficiencies even at mid-range distances (where the coupling coefficients are low) by using high Q-factor resonators (i.e., high Q-factors can

compensate for low values of the coupling coefficient). In fact, per Figure 2.6, if the coupling coefficient is smaller than 0.1 (as it is often the case in SCMR systems) then the quality factor of the TX/RX resonators would have to be equal or greater than 100 in order to obtain efficiencies higher than 80%.

CHAPTER III. MINIATURIZATION TECHNIQUES FOR CSCMR SYSYEMS

As it was seen in the previous chapter, traditional SCMR systems require a set spacing between their source/load and TX/RX loops or coils, which in turn makes them bulky. However, many applications require that WPT systems are compact; therefore, SCMR systems cannot be easily integrated in such applications. To address this problem, the Conformal SCMR (CSCMR) [32] [33] was proposed, which miniaturizes the size (i.e., volume) of traditional SCMR systems by placing the source and load loops coplanar with the TX and RX resonator loops, respectively. Due to their compact size and high efficiency, CSCMR systems are well-suited for applications where space is limited, such as, wearable and biomedical devices. Therefore, this research is based on the CSCMR method.

3.1)   Traditional CSCMR Design

A typical CSCMR system is shown in Figure 3.1, and it is composed of a TX element connected to a source, which transmits power wirelessly to an RX element that is connected to a load. Typically, the TX and RX elements are identical. Also, the TX and RX elements consist of a resonant loop placed co-planarly to a source and a load loop, respectively. In addition, lumped capacitors are connected to the resonator TX and RX loops. These lumped capacitors are chosen so that the CSCMR system operates at the frequency where the TX and RX resonators exhibit their maximum Q-factor. The resonant frequency (f_r) is found as follows:

17

$$f_r = \frac{1}{2\pi\sqrt{LC}}$$

(3.1)

where L is the self-inductance of the TX (or RX) resonant loops and C is the needed lumped capacitance. The value of C can be determined by the following equation:

$$C = \frac{1}{4\pi^2 f_r^2 L}$$

(3.2)

Furthermore, the self-inductance of each loop can be calculated using the following [4]:

$$L = \mu_0 r \left[\ln\left(\frac{8r}{r_c}\right) - 2 \right]$$

(4)

where μ_0 is the permeability in free space, r is the radius of loop, and r_c is the cross-sectional radius of the loop.
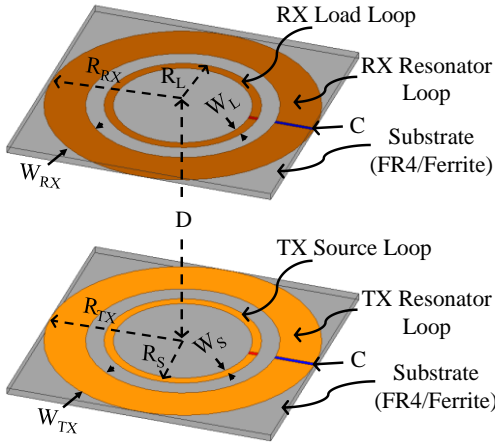
Figure 3.1. Typical CSCMR system

3.2)   Miniaturization and Optimization of CSCMR Systems

In this section, we aim to design a miniaturized CSCMR system. To achieve this, the width of the resonant loop is increased toward the source/load loops while maintaining the overall footprint (i.e., area size) of a reference design (see TABLE 3. I). As the width of the resonant loops increases towards the source/load loops: (a) the CSCMR system's stray capacitance also increases since the distance between source and load loops and their

18

corresponding resonators decreases, and (b) the resonators' self-inductance increases. This leads to the miniaturization of the CSCMR system since based on (3.1) the operational frequency is inversely proportional to the product of the capacitance and inductance (i.e., lowering the frequency while maintaining the same physical size is equivalent to miniaturization). To maintain the same footprint while increasing the width of the resonators, we simultaneously decrease the width of the source/load loops.

TABLE 3. I. TRADITIONAL CSCMR DESIGN PARAMETERS

Parameter	Value
Inner radius of source/load loop ($r_{Sin} = r_{Lin}$)	13 mm
Width of loops ($W_{TX} = W_{RX} = W_S = W_L$)	6 mm
Inner radius of TX/RX resonator loop (r_{TXin}, r_{RXin})	26 mm
Distance between TX and RX (D)	60 mm
Lumped Capacitance (C)	33 pF

The performance of CSCMR design is analyzed using simulations in ANSYS HFSS for W_S ($W_L = W_S$) of 6 mm, 4 mm, and 2 mm and varying the width of the TX/RX resonator loops W_{TX} ($W_{RX} = W_{TX}$) for two different values of $r_{Sin} = 13$ mm and $r_{Sin} = 15$ mm, as shown in Figure 3.2(a) and Figure 3.2(b), respectively. Each square point represents the maximum efficiency of each CSCMR design (i.e., representing a different W_{TX}) at its resonant frequency. Each line is formed by varying W_{TX}, starting at higher frequency values (at the right of the graphs) with a W_{TX} of 6 mm, 8 mm, and 10mm for the black, red, and blue lines, respectively for Figure 3.2(a), and a W_{TX} of 4 mm, 6 mm, and 8mm for the black, red, and blue lines, respectively for Figure 3.2(b). In each line, the W_{TX} is increased inwardly (i.e., towards source/load loops) by a step of 1 mm, until the gap between the source/load loops and resonator loops reaches 1 mm. For each of the scenarios described above, the frequencies, where each system provides the highest efficiency are plotted. The lumped capacitors, C, were optimized in each configuration to provide maximum Q-factor

thereby achieving the highest efficiency. The distance between the TX and RX, D, and outer radius of the resonator loops r_{TX}, r_{RX} are kept constant throughout.

By increasing the resonator loop widths W_{TX} towards the source/load loops, the miniaturization of CSCMR systems is achieved. Let us consider the reference CSCMR design (the first square on the right of the black line) shown in Figure 3.2a, where $W_{TX} = W_S = 6$ mm and $r_{Sin} = 13$ mm. The operating frequency of this system is 88 MHz with a PTE of 89.4%. When W_{TX} is increased to 9 mm and $r_{Sin} = 13$ mm (the fourth square from the right end of the black line), the operating frequency reduces to 46 MHz and system's PTE is 87.71%. Therefore, with these new parameters, the CSCMR system can operate at significantly lower frequency while providing a PTE that is almost the same with the reference design (only a 2% decrease in efficiency occurs). Operating at a lower frequency while maintaining the same footprint is equivalent to miniaturization, as at lower frequencies the wavelength is larger, and the same design becomes electrically smaller. In fact, the design achieves approximately the same efficiency with the reference design but at a notably lower frequency while keeping the same size with the reference design.

By reducing the width of the source/load loops, more space is available to accommodate the increase of the resonator width. The blue lines in Figure 3.2 illustrate the CSCMR designs that have a source/load loop width of 2 mm. By increasing the width of the resonators, the CSCMR system's self-inductance and the stray capacitance increase, which causes the operational frequency to decrease. By comparing the lowest achieved frequency of the blue line ($W_{TX} = 2$ mm) to the black line ($W_{TX} = 6$ mm), it is seen that the $W_{TX} = 2$ mm design achieves a higher PTE of 74.42% (compared to 71.9%) at the lower frequency of 15.09 MHz (compared to 18.96 MHz). Further, the PTE of the blue line is

higher across all points than the red and black lines. Additionally, simulation results, which are not presented here for brevity, indicate that further miniaturization is possible by further increasing r_{Sin} for a $W_S = 2$ mm, and by also further reducing W_S.

Finally, by comparing the cases, where the source/load loops inner radius r_{Sin} is 13 mm (Figure 3.2a.) and 15 mm (Figure 3.2b.), respectively, an interesting observation is made. When $r_{Sin} = 13$ mm, the CSCMR systems operate with better PTE at higher frequencies, i.e., beyond 40MHz compared to when $r_{Sin} = 15$ mm. Below 40 MHz, the CSCMR systems with $r_{Sin} = 15$ mm, PTE is improved over $r_{Sin} = 13$ mm. Therefore, it may also be concluded that by increasing the inner radius, we can increase the PTE at low frequencies, whereas a higher value for r_{Sin} improves the PTE at higher frequencies.
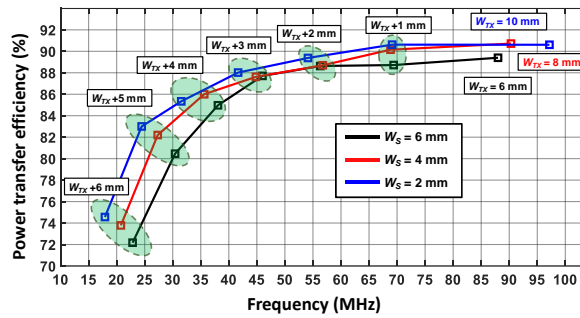
(a)
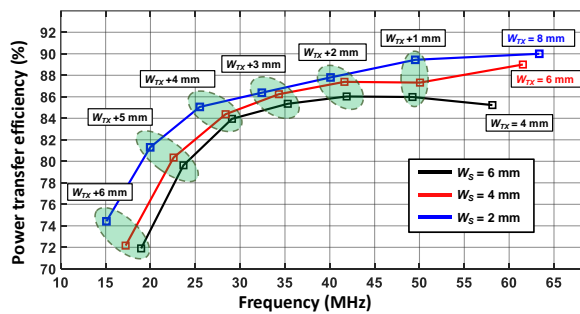
(b)

Figure 3.2. Simulated PTE of CSCMR systems for varying W_{TX} with (a) inner radius of source loop $r_{Sin} = 13$ mm and (b) an inner radius of source loop $r_{Sin} = 15$ mm.

A.) Fabrication and Measurements

To verify the simulated results in the previous section, three CSCMR types were fabricated and their PTEs were measured. CSCMR A is the reference case with parameters $W_S = W_{TX} = 6$ mm. Then, CSCMR B is the system with parameters of $W_S = 6$ mm and $W_{TX} = 9$ mm. Lastly, CSCMR C is the system with parameters $W_S = 2$ mm and $W_{TX} = 15$ mm. The measured PTE of the three CSCMR A, B and C systems are illustrated by the black, red and blue line in Figure 3.2, respectively. All these systems have a $r_{Sin} = 13$ mm, diameter of 64 mm, and operate for a TX/RX distance of 60 mm. A thin Kapton® ($\varepsilon_r = 3.34$; thickness of 0.05 mm) film is used as a substrate material. The PTE, η, of the different systems were measured using a Keysight Vector Network Analyzer (VNA) and it is defined as $\eta = |S_{12}|^2$.

CSCMR A exhibits a peak measured PTE of 76.12 % at its resonant frequency of 83.2 MHz, whereas its simulated PTE peak of 89.4% occurs at 88 MHz. CSCMR B exhibits a peak measured PTE of 75.57 % at its resonant frequency of 44.6 MHz, whereas its simulated PTE peak of 87.71% occurs at 46 MHz. CSCMR C exhibits a peak measured PTE of 70.1% at its resonant frequency of 23.75 MHz, whereas its simulated PTE peak of 83% occurs at 24.46 MHz. The slight differences in the measured and simulated PTEs and resonant frequencies are attributed to fabrication errors and losses due to effective series resistance (ESR) of capacitors, which is not modeled in our simulations. The measured results of Figure 3.3 verify the conclusions of our simulation analysis by clearly showing that by increasing the width of the resonators CSCMR systems can achieve high PTEs at low operating frequencies.
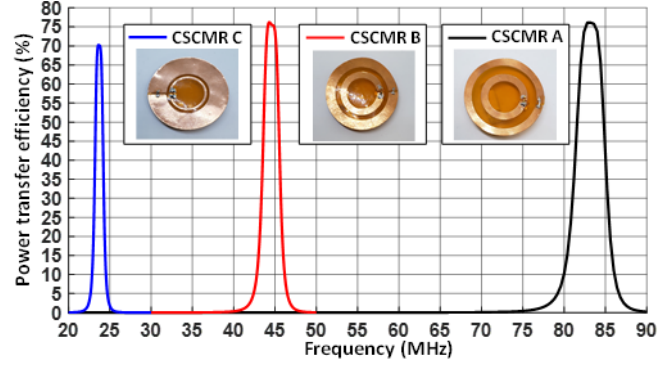
Figure 3.3. Measured PTE of CSCMR system with: (A) W_S = 6 mm and W_{TX} = 6 mm (reference), (B) W_S = 6 mm and W_{TX} = 9 mm, and (C) W_S = 2 mm and W_{TX} = 15 mm.

3.3)   Miniaturization and Enhanced WPT systems via Ferromagnetic Substrates

While CSCMR systems can reduce volume significantly, further miniaturization may still be realized using other methods such as utilizing metamaterials and ferrites. Additionally, in the presence of metallic objects, traditional SCMR systems suffer significant losses in efficiency because metallic objects block electromagnetic fields and in turn diminish the coupling between TX and RX [34]. This is an important problem for many applications that need to utilize WPT systems on or nearby metallic bodies. In this section, ferromagnetic materials are used to miniaturize CSCMR systems and isolate the effects of metallic objects on such systems.

A.) CSCMR with Ferrite Substrate

TABLE 3. II. CSCMR DESIGN PARAMETERS

Parameter	Value
Inner radius of source/load loop (r_{Sin} = r_{Lin})	13 mm
Width of loops (W_{TX} = W_{RX} = W_S = W_L)	6 mm
Inner radius of TX/RX resonator loop (r_{TXin}, r_{RXin})	24 mm
Distance between TX and RX (D)	60 mm
Thickness of substrate / ferrite (T_s)	0.5 / 1.5 mm

23

The CSCMR system is based upon the same design as in Figure 3.1 but instead of using a traditional substrate (i.e. FR-4), it utilizes a ferromagnetic substrate. The geometrical parameters of the system used are given by TABLE 3. II. A 0.5 mm or a 1.5 mm thick ferrite sheet with $\mu_r = 45$, $\varepsilon_r = 12$ and $\tan \delta_\mu = 0.2222$ is placed under the TX and RX elements as shown in Figure 3.4. Also, a thin Kapton film with $\varepsilon_r = 3.34$ and thickness of 0.05 mm is placed between the resonators of the TX and RX and their ferrite substrates. The measured and simulated results of the CSCMR system with and without ferrite are compared in Figure 3.5. These results show that by adding a ferrite substrate under the CSCMR system, which was initially operating at 40 MHz, we can reduce its operating frequency to 33.5 MHz and 32 MHz for 0.5 mm and 1.5 mm thick ferrite sheet, respectively. This reduction of operating frequency is achieved while maintaining the same dimensions, thereby miniaturizing the WPT system. The slight efficiency drop in measurements could be attributed to: (a) possible differences between the ferrite's magnetic loss used in our simulations versus the actual one, and (b) fabrication errors.

(a)   (b)

Figure 3.4. Fabricated CSCMR (a) with ferrite substrates in air, (b) with ferrite substrates over a metallic surface.
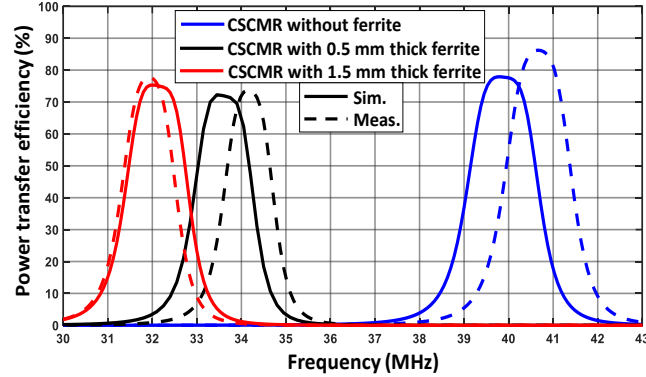
Figure 3.5. Comparison between simulation and measurements of CSCMR system with and without ferrite sheet.

B.) CSCMR on a Metallic Surface

Previous works have shown that a significant decrease in the transfer efficiency becomes apparent in the presence of metallic objects [34]. This is the same for our CSCMR system. Specifically, the transfer efficiency of our system is approximately zero when a square 120 mm x 120 mm copper sheet is placed below the RX at a distance of 0.5 mm or 1.5 mm. However, when a ferrite sheet of 0.5 mm or 1.5 mm thickness is placed under both TX and RX elements [on top of the metallic surface, as shown in Figure 3.4(b)], the transmission efficiency increases significantly. Figure 3.6 compares the simulated and measured results for on CSCMR system with the ferrite substrates over a metallic surface. When a 0.5 mm thick ferrite sheet is used, the resonant frequency increases to 36.4 MHz with a PTE of 37.3%. Also, with a 1.5 mm thick ferrite sheet, the operating frequency is 32 MHz and the PTE increases to 62.9%. Therefore, ferromagnetic materials can confine the magnetic flux linkage of the CSCMR system. In addition, using thicker ferrite substrates significantly mitigates the losses of CSCMR systems due to the presence of metallic surface.
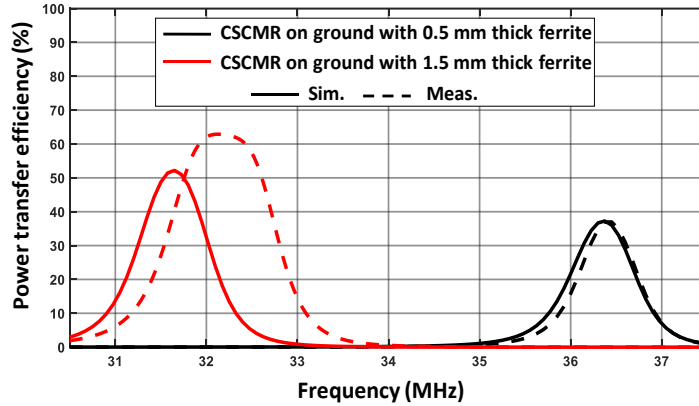
Figure 3.6. Measured and simulated PTE of CSCMR system with ferrite sheets over a metallic surface.

3.4) Conclusion

Highly efficient and miniaturized CSCMR systems were developed by increasing the widths of TX and RX resonant loops and reducing the widths of source/load loops. Our results indicate that the maximum PTEs are achieved by using 2-mm wide source/load loops in our CSCMR systems. Furthermore, the inner radius of source/load loops can be varied to optimize the CSCMR system's performance even further depending on the operating frequency.

Also, ferromagnetic materials can be used to enhance the performance of CSCMR systems. The high permeability properties of ferrites lead to CSCMR systems with high-quality factors at lower frequencies, thus miniaturizing such systems. Also, ferrites can be used to isolate CSCMR systems from metallic surfaces by confining magnetic flux linkage.

CHAPTER IV. RANGE EXTENSION VIA A PLANAR RELAY RESONATOR

SCMR and CSCMR provide efficient WPT at maximum distances in the order of the size of the resonators used at the TX and RX elements. Beyond this optimal transmission range, the efficiency of SCMR systems drops very quickly. In fact, extending the range of SCMR is challenging and it is also needed for several applications. Therefore, new designs that can extend the range of CSCMR systems will be explored in this chapter.

Different approaches have been previously used to extend the range of WPT systems. Passive repeater coils in a domino arrangement have been used in [35] [36]. Even though relay resonators can increase the PTE at longer distances, in many applications their use is not practical as these additional resonators use a substantial amount of space directly along the power transmission path. To remedy these limitations, [37] introduced a single repeater resonator that was labeled as "U-coil". This U-coil repeater is planar along the transfer distance and perpendicular between the TX/RX coils. The U-coil greatly amplified the efficiency of an IPT two-coil system at a transfer distance of 1m by a multiple of ten. A similar approach was used in [38], where TX and RX elements, which are coplanar to multiple U-coil resonators, were used to direct the transfer of power wirelessly at a distance of over 5 m, while still attaining a high efficiency of over 50%. Furthermore, WPT systems that are enhanced with U-coils can be used to transfer power in applications where resonators in domino arrangements are not suitable, especially where the space between TX and RX cannot have any obstructions. Such applications include charging of home/kitchen appliances and mobile/wearable devices.

In this thesis, a simpler relay resonator (known as the U-loop) is used to achieve the following: (a) increase the PTE at longer distances, i.e., extend the WPT range, (b)

provide misalignment insensitivity, and (c) provide consistently high PTE along various locations around and within the U-loop. Notably, this work advances the designs of [37], [38] by: (a) utilizing a CSCMR method of WPT instead of an IPT method, (b) introducing a simpler and easier to manufacture passive resonator loop instead of a large resonant coil, and (c) studying the performance of the proposed WPT system for different locations of the RX in respect to the U-loop. The techniques used for the extension of WPT systems in this section have not been explored previously.

4.1)   Proposed Design

The traditional CSCMR system with identical TX and RX elements is the same as shown in Figure 3.1. The TX (or RX) element consists of a source (or load) loop coplanar with a resonator loop that is terminated on a lumped capacitor. The capacitor is chosen to resonate the system at its maximum quality factor (Q-factor). A 180 pF lumped capacitor (C) was used for our design. Our proposed CSCMR system with a U-loop is depicted in Figure 4.1. The U-loop is a single loop of 60 mm radius and a lumped capacitor (C_U) that is determined by the system's maximum Q-factor condition. All the geometrical parameters of our CSCMR system with the U-loop are as follows: $R_S = R_L = 19$ mm, $W_S = W_L = 6$ mm, $R_U = 60$ mm, $R_{TX} = R_{RX} = 30$ mm, $W_{TX} = W_{RX} = W_U = 7$ mm, $D_U = 120$ mm and $D = 60$ mm.
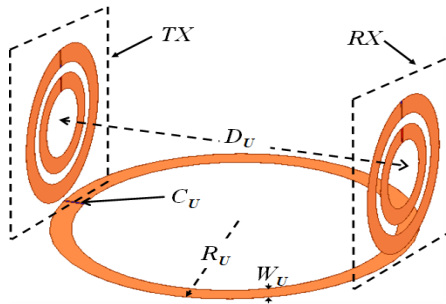
Figure 4.1. Proposed CSCMR with U-loop.

CSCMR is based on the magnetic resonance principle, which was introduced by [15]. Such

28

resonant structures require high reactance to resistance ratios which can be described as Q-factor [39]. The Q-factor is the ratio of energy stored to energy lost. Therefore, high Q-factor for TX and RX CSCMR elements are needed to achieve high efficiencies. By adding relay resonators, the mutual couplings of a WPT system increases and the number of resonant modes also increases [15]. The equivalent circuit of a CSCMR structure with multiple resonators (see Figure 4.2) can be described by the following matrix [32], [40]-[41]:

$$
\begin{bmatrix} V_S \\ 0 \\ 0 \\ 0 \\ 0 \end{bmatrix} = \begin{bmatrix} Z_S & j\omega M_{1,2} & j\omega M_{1,3} & j\omega M_{1,4} & j\omega M_{1,5} \\ j\omega M_{2,1} & Z_2 & j\omega M_{2,3} & j\omega M_{2,4} & j\omega M_{2,5} \\ j\omega M_{3,1} & j\omega M_{3,2} & Z_3 & j\omega M_{3,4} & j\omega M_{3,5} \\ j\omega M_{4,1} & j\omega M_{4,2} & j\omega M_{4,3} & Z_4 & j\omega M_{4,5} \\ j\omega M_{5,1} & j\omega M_{5,2} & j\omega M_{5,3} & j\omega M_{5,4} & Z_L \end{bmatrix} \begin{bmatrix} I_S \\ I_2 \\ I_3 \\ I_4 \\ I_L \end{bmatrix} \qquad (4.1)
$$
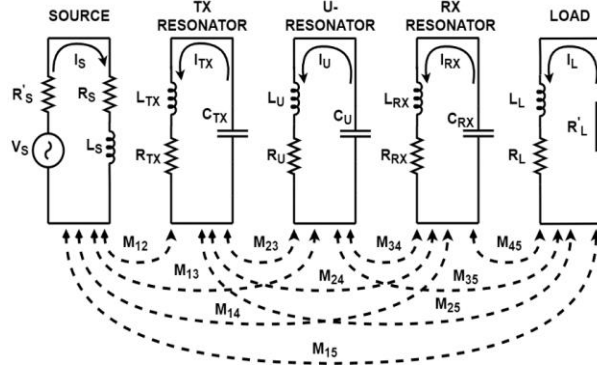
Figure 4.2. Equivalent circuit model of CSCMR with U-loop resonator.

where V_S, ω, $M_{n,m}$, I, and Z are the voltage of the source, angular frequency, mutual inductance, current, and self-impedance, respectively (the subscripts n, S and L represent n^{th} resonator, source and load loops, respectively). For the interested reader, a detailed analytical model that predicts the efficiency of CSCMR systems with multiple resonators can be found in [32].

The prototype of the proposed design is depicted in Figure 4.3. The U-loop relay resonator, as well as the TX and the RX elements of our design, are constructed on a thin Kapton® film substrate with $\varepsilon_r = 3.34$ and thickness of 0.05 mm. The efficiency, η, of our system was measured using a Keysight Vector Network Analyzer (VNA) and it was defined as $\eta = |S12|^2$. All simulations were performed using ANSYS HFSS.

Figure 4.3. Prototype of the proposed CSCMR system with a simplified U-loop.

First, the efficiency of the CSCMR system of Figure 3.1 without the U-loop (i.e., traditional CSCMR system) is measured and simulated. Figure 4.4 shows these results for different TX/RX distances, D, between 60 mm to 140 mm. It is clearly seen that beyond a transfer distance of 80 mm, the efficiency begins to significantly decrease by approximately a factor of two per 20 mm. This illustrates that traditional CSCMR systems provide a limited range, which is typically equal to the maximum dimension of the resonator (this is also the case for SCMR systems). Therefore, there is a need for a new method that can extend the range of CSCMR systems. This is achieved in the following

section by adding the U-loop. The slight difference between the simulated and measured resonant frequency can be attributed to fabrication errors.
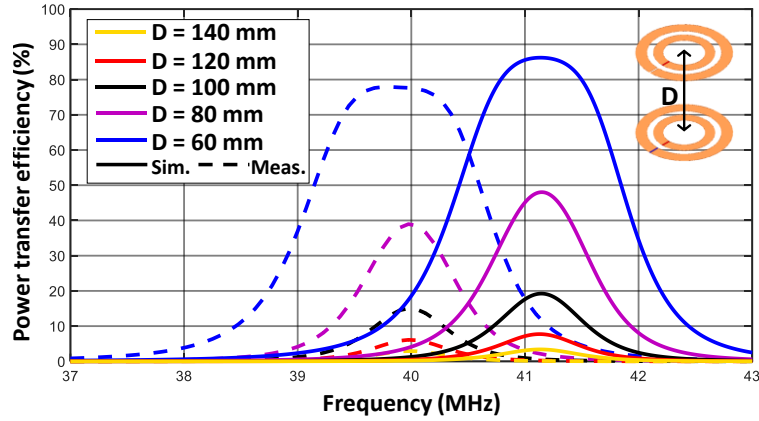
Figure 4.4. Measured and simulated efficiency of the traditional CSCMR system at various distances, D.

The measured and simulated results of the proposed CSCMR system with the U-loop (shown in Figure 4.3) are compared at different distances, D, from D_{min} = 60 mm to D_{max} = 140 mm (as shown in Figure 4.5) for a lumped capacitor, C_U, of 56 pF and 82 pF in Figures 4.6(a) and 4.6(b), respectively. These results show that the main resonance of the system occurs at a different frequency depending on the value of C_U. For both values of C_U, the proposed CSCMR system provides maximum efficiency of 73% at an extended range of D_U = 120 mm and near the resonant frequency of the original CSCMR system without the U-loop (i.e., 40 MHz). Furthermore, for a range between 100–120 mm, the proposed CSCMR system with the U-loop maintains an efficiency that is higher than 60%. Also, this system provides high efficiency at the original transfer distance of 60 mm.
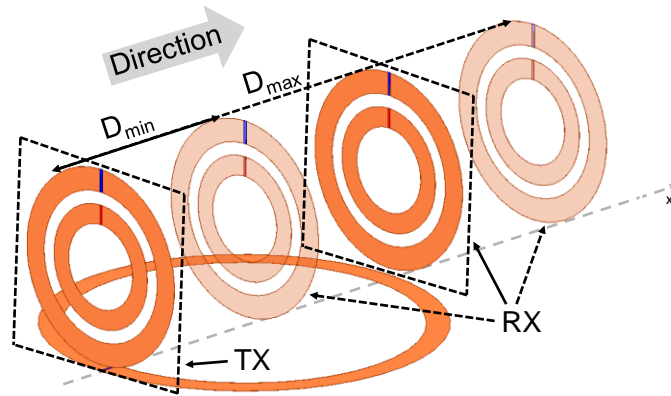
Figure 4.5. 3-D view of the CSCMR system with the U-loop for distances between TX and RX of D_{min}, D_U, and D_{max}.
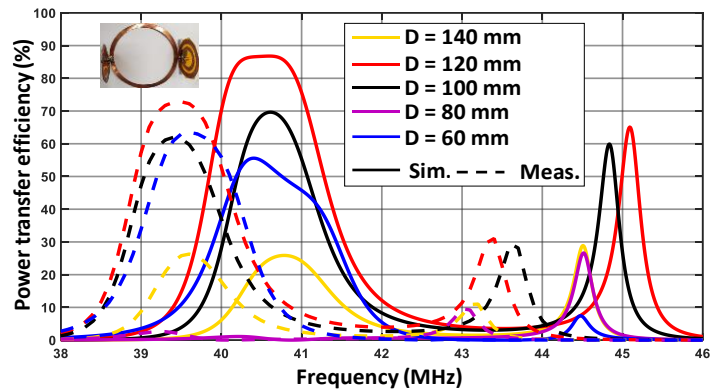
(a)
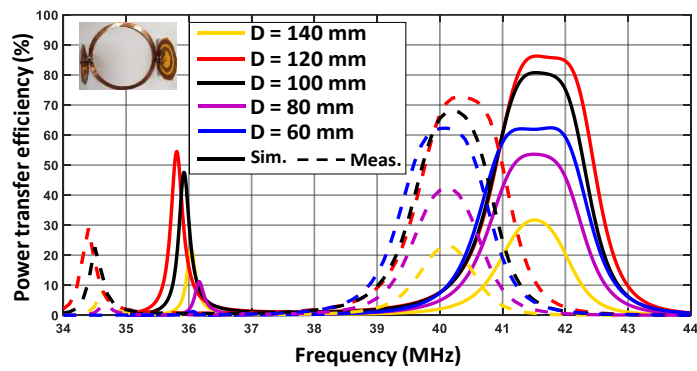
(b)

Figure 4.6. Measured and simulated efficiency of CSCMR system with U-loop at various distances and for a lumped capacitor (a) $C_U = 56$ pF and (b) $C_U = 82$ pF.

In conclusion, the proposed CSCMR system provides higher efficiency than the traditional CSCMR system for distances that are longer than 80 mm. Specifically, at 120 mm the proposed system has an efficiency that is 10 times higher than the one of the traditional systems. Moreover, the traditional CSCMR system exhibits higher efficiency than the proposed CSCMR system only at 60 mm. Specifically, the efficiency of the systems with and without the U-loop are 60% and 80%, respectively. Notably, at $D = 80$ mm, the proposed CSCMR system with $C_U = 56$ pF exhibits approximately zero efficiency near the original operating frequency, whereas the system with $C_U = 82$ pF exhibits a 40% efficiency. This implies that the capacitor of the U-loop affects the efficiency of the system depending on the distances and needs to be carefully picked depending on the application. Also, based on the results of Figures 4.6(a) and 4.6(b), it can be seen that a second resonance appears due to the presence of the U-loop. This phenomenon was studied in detail by [42], which proved that the insertion of an odd number of relay resonators introduces three split resonant modes. At first glance, the PTE responses in Figures 4.6(a) and 4.6(b) seem to show only two resonant modes. However, upon closer examination, it is understood that the third resonant mode is not visible in these cases as two of the resonances have converged to the same frequency.
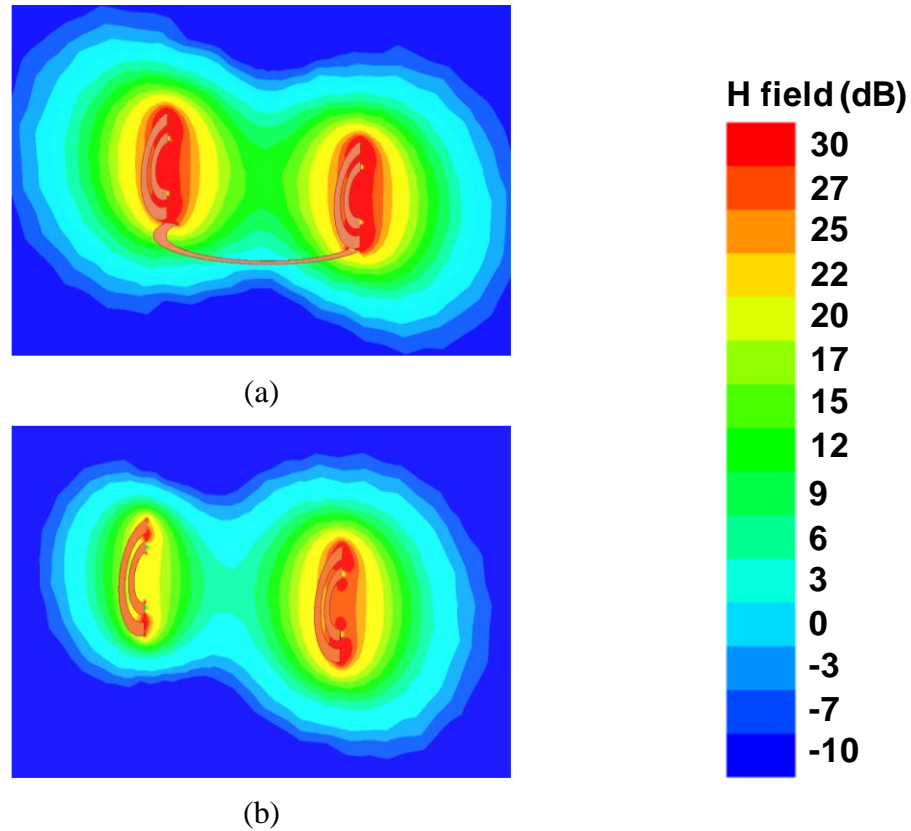
Figure 4.7. Magnetic-field distribution of CSCMR system at the resonance frequency for a distance of 120 mm (a) with U-loop and (b) without U-loop.

The magnetic field intensities (H-field) of the CSCMR systems with and without U-loop at their respective simulated resonance frequencies of 41.2 MHz and 41.4MHz and distance $D = 120$ mm are illustrated in Figure 4.7(a) and 4.7(b). WPT systems require high magnetic flux through the TX and RX elements in order to provide high efficiency. The field distributions in Figure 4.7 show that in the area between the two coupled TX/RX loops, the H-field intensity of the system without the U-loop is significantly smaller than the one with the U-loop. This indicates that the magnetic flux through the TX/RX loops is low thereby explaining the low efficiency of the traditional CSCMR system (i.e., without the U-loop) at this distance. However, in our proposed system, the U-loop allows the magnetic flux to pass through it thereby establishing strong coupling of the TX/RX

resonators and in turn providing high efficiency at the distance of 120 mm. The process in which the U-loop can facilitate the power transfer can be explained by Faraday's law of induction, based on a change in the magnetic field (flux) going through a conductive loop or coil which induces an electromotive force (EMF), which in turn induces a current on the conductor [43]. In our case, the power source is exciting the source loop with an electric current, which creates a time-varying magnetic field (as described by Ampere's law [43]). This field induces an EMF that enables the TX to efficiently couple its energy to the U-loop. Also, this coupling occurs between the U-loop and the RX, thereby enabling us to efficiently transfer power from the TX to the RX at extended distances.

4.2)   Effect of Increasing the U-loop Diameter and Transfer Distance

In this section, the diameter of the U-loop is increased using a step of 60 mm. The starting case at 60 mm distance does not have a U-loop. All, other cases have a U-loop with a diameter that is equal to the distance between the TX and RX resonators (D_U). In our simulations, the maximum D_U is 720 mm, while in our measurements the maximum D_U is 360 mm. This maximum distance in our measurements was determined by the maximum U-loop that we could accurately fabricate in our laboratory. Notably, the frequency at which each design achieved its maximum efficiency was not always exactly the same, but all of them were within the range of 41±0.5 MHz in simulations and 40±0.5 MHz in measurements. The measured efficiency is approximately 15% less than the simulated one. This is attributed to: (a) the losses of the capacitors that are not included in our simulations, as they are simulated as ideal lossless elements, and (b) fabrication tolerances of our prototypes.
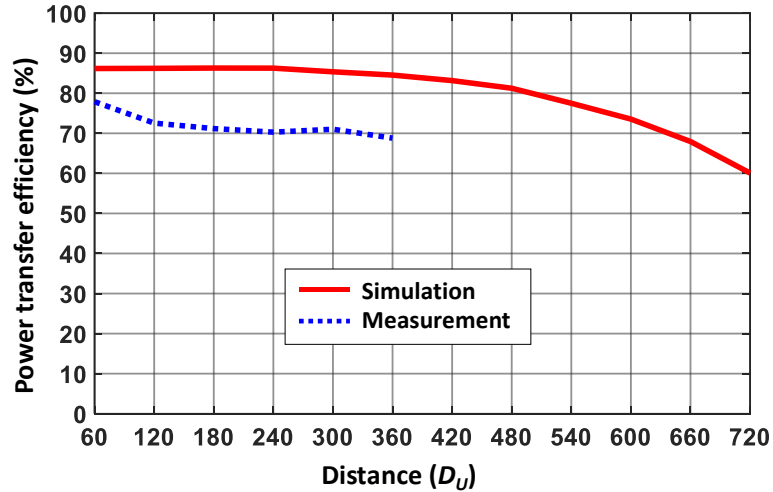
Figure 4.8. Measured and simulated efficiency of CSCMR systems with U-loop at various distances, D_U, that are equal to the diameter of the U-loop.

The simulated and measured efficiency at various distances, D_U, (and corresponding equal U-loop diameters) are compared in Figure 4.8. The simulated results indicate that for distances larger than 480 mm the efficiency begins to decay and drops down to approximately 60% at the maximum distance of 720 mm. However, at transfer distances below 480 mm, the simulated efficiency remains higher than 80%. A slight discrepancy occurs between simulation and measurements when the U-loop is absent (60 mm). Specifically, in simulations the addition of the U-loop does not immediately cause a drop in efficiency, whereas in measurements a drop of around 5% is encountered. This small difference is attributed to compounding fabrication and capacitor losses.

A.) RX Oriented Parallel with U-loop

Here, the proposed CSCMR system's RX is parallel to the U-loop. Specifically, the RX is positioned 10 mm above the U-loop and measurements are conducted at different locations within the U-loop with $R_U = 120$ mm, as shown in Figure 4.9. The TX is perpendicular to the U-loop as in previous scenarios (see Figure 4.9).
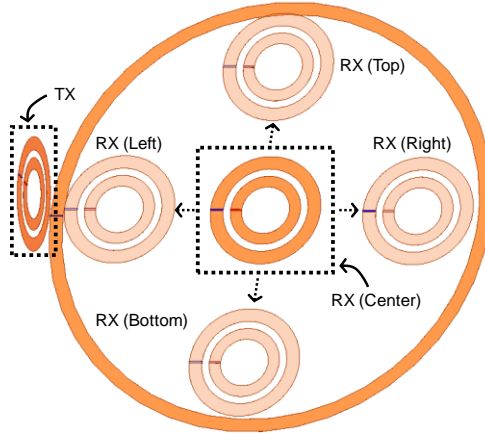
Figure 4.9. RX is parallel to the U-loop and it is placed at various positions within a U-loop with $R_U = 120$ mm.

The measured results for top, center, right, bottom and left locations (see Figure 4.9) are plotted in Figure 4.10. The results demonstrate that any location within the U-loop, the proposed CSMCR system exhibits approximately the same response. The largest deviation occurs when the RX is placed at the left side location of the U-loop. In all other cases, the efficiency of the system at the resonant frequency of 40 MHz is between 69% and 72%. These results are especially applicable for mobile device and drone charging and can lead to the development of wireless charging pads that cover significantly large areas.
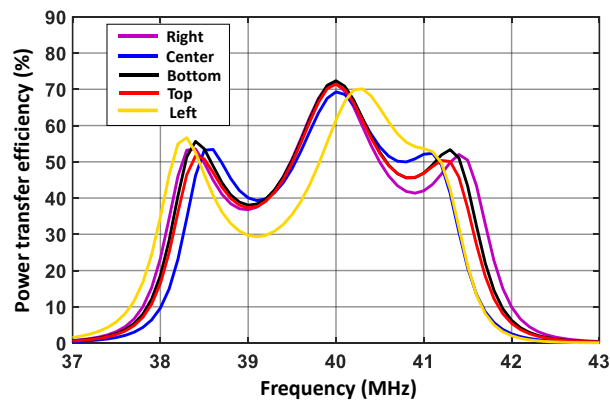
Figure 4.10. Measured efficiency for the cases shown in Figure 4.9.

B.) Analysis of Resonant Modes

As mentioned previously, the addition of the U-loop resonator can generate three resonances. The three different resonant modes shift in frequency depending on the lumped capacitor of the U-loop. This is shown in the simulated results depicted in Figure 4.11. For $C_U = 55$ pF, two of the resonant modes converge to the same frequency of 40.5 MHz, and the other resonant frequency peak occurs at 45.5 MHz with significantly lowered PTE. When the lumped capacitor of the U-loop increases to $C_U = 65$ pF, three distinct resonances appear at 38.75 MHz, 40.75 MHz and 43MHz and they exhibit similar peak efficiencies. Also, when the lumped capacitor further increases to $C_U = 75$ pF, two resonances start to converge at the same frequency of 41.5 MHz, while the other peak shifts downward at just under 37 MHz with a slightly lower PTE.
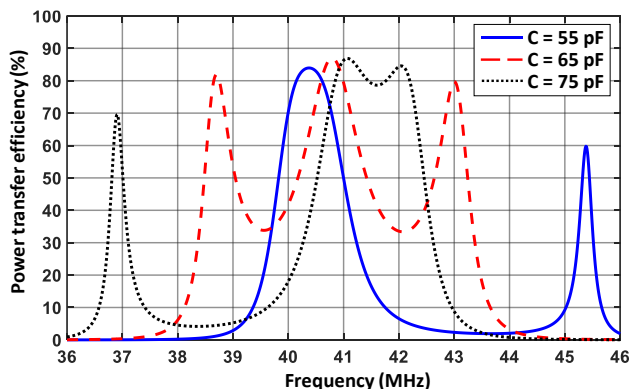
Figure 4.11. Simulated efficiency of CSCMR system with U-loop of varying lumped capacitance.

C.) Misalignment Insensitivity

This section studies the performance of the proposed CSCMR system for various angular positions of the RX around the U-loop, as shown in Figure 4.12. Specifically, the RX was placed at angular positions from $\theta = -120°$, to $\theta = 120°$ around the U-loop. The corresponding simulated and measured efficiencies at these positions are shown in

Figure 4.13. The measured efficiency is approximately 15% less than the simulated one due to the losses of the capacitors that are not included in our simulations (as they are simulated as ideal lossless elements) and fabrication tolerances of our prototypes. Due to the U-loop's symmetry, the same response is expected at their corresponding opposite angles (i.e., the cases for $\theta = -90°$ and $\theta = 90°$ will exhibit the same efficiency). The results shown in Figure 4.13, indicate that the measured efficiency of our CSCMR system remains higher than 70% for angular positions, θ, between -90° and 90° and for both values of the U-loop's capacitor. However, for values below $\theta = -105°$ and values above $\theta = 105°$, our CSCMR system with $C_U = 82$ pF experiences a frequency split, which reduces its efficiency to approximately 65%, as shown in Figure 4.13(b). On the contrary, for these angular positions, the system with $C_U = 56$ pF experiences a significant reduction in its efficiency to approximately 10%, as shown in Figure 4.13(a). These results reinforce the idea that the capacitor of the U-loop affects the system's efficiency not only at different distances but also at different angular positions.
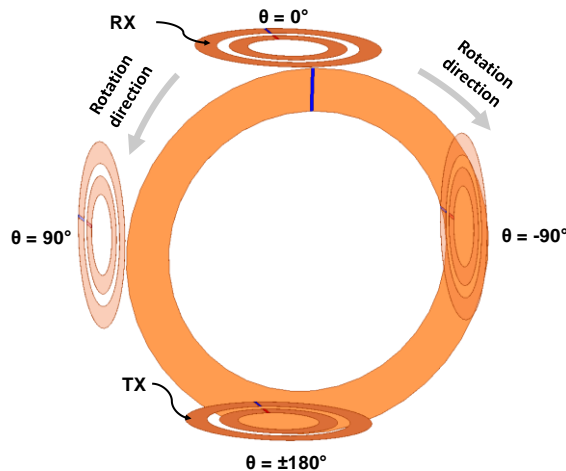
Figure 4.12. 3-D view of CSCMR system with U-loop for different angular positions of the RX around the U-loop.
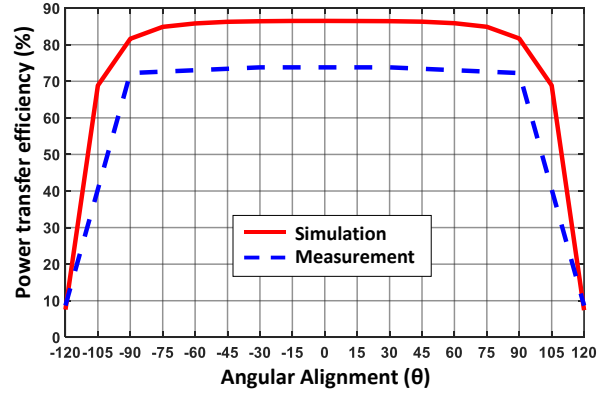
(a)
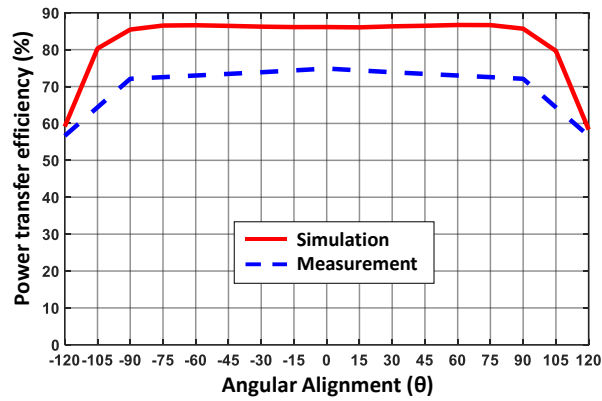
(b)

Figure 4.13. Measured and simulated efficiency of the proposed CSCMR system at various angular alignments around the U-loop for a lumped capacitor: (a) $C_U =$ 56 pF, and (b) $C_U =$ 82 pF.

4.3) Conclusion

This section studies a U-loop repeater resonator, which was proposed by [37] and [38], in CSCMR systems and closely examines the performance of these systems. The novelty of our work compared to [37] and [38] is supported by the following points: (a) CSCMR is used here instead of inductive coupling, (b) a simple and easy to fabricate loop resonator is proposed here instead of a resonator coil that occupies significantly larger volume, and (c) the performance of our proposed system for different positions and

orientations of the RX around and within the U-loop is thoroughly studied. Our results show that the U-loop resonator extends the optimal transmission distance and performs significantly better than a traditional CSCMR system at distances beyond 80 mm. Also, the proposed system maintains efficiency above 60% for a range of angular positions (θ between -120° and 120°) of the RX around the U-loop. Furthermore, when the RX is parallel to the U-loop, our system still provides high-efficiency for all locations within the U-loop. Therefore, our proposed CSCMR system with the U-loop can be applicable for charging mobile devices, which are placed parallel as well as perpendicular to the charging pad. This would provide more freedom to the users that charge their devices. Finally, the lumped capacitor of the U-loop influences the performance of this system in terms of its resonant frequency and efficiency at various distances and angular positions of the RX.

CHAPTER V. THE EFFECTS OF WEARABLE AND IMPLANTABLE DEVICES ON THE HUMAN BODY

Wireless charging is very advantageous for implantable devices as it can charge batteries without the use of wires, thereby significantly extending the lifetime of such devices and eliminating the infection risks of transcutaneous wires. Additionally, WPT eliminates the need for costly and possibly difficult surgeries, which have health risks for patients, to replace implantable devices after their batteries have been depleted [44]. Furthermore, wearable sensors, which can be wirelessly charged, are very useful for health monitoring and diagnostics. However, the Power Transfer Efficiency (PTE) of WPT systems decreases when they are placed on or inside the human body due to the absorption of the electromagnetic fields (EMFs) by human tissues [45]. This is a significant challenge that must be addressed to enable the development of future wire-free implantable and wearable devices. Therefore, this thesis aims to study and quantify the impact of different parts of the human body on the performance of wearable and implantable WPT systems. Furthermore, this chapter introduces a solution to mitigate the losses due to the proximity of the WPT system to the human body. Specifically, this reduction is achieved by using ferromagnetic (ferrite) substrates, instead of other traditional substrates.

5.1) Proposed Design for Wearable Applications

A CSCMR system (see Figure 3.1) is designed to operate at the Industrial, Scientific, and Medical (ISM) band of 27.12 MHz. This system uses a capacitor, C, of 470 pF or 280 pF for FR-4 and ferrite substrates, respectively. Specifically, in this design, the width of the source/load loops was 2 mm. This allowed us to use resonant loops with larger width and achieve significantly higher PTE than previous CSCMR systems. All the

geometrical parameters of our optimized CSCMR system are given as follows: $R_S = R_L = 17$ mm, $W_S = W_L = 2$ mm, $R_{TX} = R_{RX} = 30$ mm, $W_{TX} = W_{RX} = 9$ mm and $D = 60$ mm. Two sets of TX and RX CSCMR units were fabricated and measured in free space. The first pair was printed on a 1.5mm-thick FR-4 substrate and its performance is used as a benchmark. The second pair was printed on a flexible ferrite sheet [46] with $\mu_r = 45$, $\varepsilon_r = 12$ and $\tan \delta_\mu = 0. 0.007$ at 27.12 MHz. For a fair comparison, three stacked layers of 0.5mm-thick ferrite sheets are used to form a 1.5 mm-thick ferrite substrate. The measurements and simulations of the CSCMR system on the FR-4 are compared in Figure 5.1. The CSCMR on FR-4 exhibits a simulated and measured efficiency of 73.43% and 70.0%, respectively. This difference in PTE between measurements and simulations is attributed to fabrication errors that are not modeled in ANSYS HFSS. It should be noted that the material properties of the ferrite substrate were not fully and accurately defined at the 27.12 MHz in the specification of the material. We chose to adjust our ferrite's material properties μ_r, ε_r and $\tan \delta_\mu$ to the values defined above so that our simulation agreed well with the measurements. This is acceptable because the goal is to evaluate the relative effects that different parts of the human body have in the performance of CSCMR systems. Therefore, the simulation model of the CSCMR system with the ferrite substrate in free space (which we created and validated using these material properties) will serve as the basis for simulating the performance of this system on various parts of the human body. The simulated and measured results for the CSCMR system with the ferrite substrate are 75.27% and 71.0% PTE, respectively (see Figure 5.1).
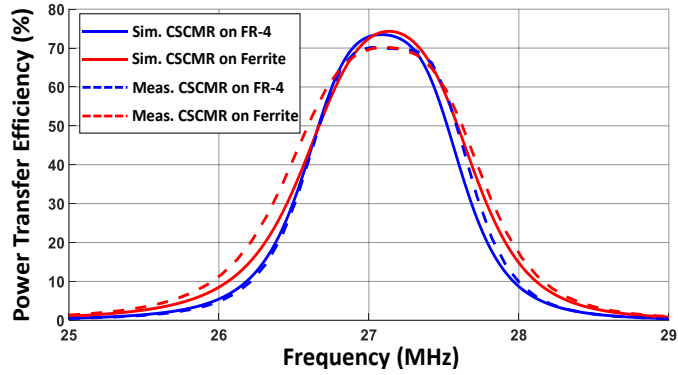
Figure 5.1. Simulated and measured PTE of CSCMR system versus frequency in free space.

The magnetic field distributions (H-field) of the CSCMR system on FR-4 and ferrite substrates are shown in Figure 5.2(a) and 5.2(b), respectively. It is clearly seen that the magnetic field distributions of these two CSCMR systems are different. The ferrite substrate confines the magnetic fields and reduces their intensity behind them. This behavior explains why ferromagnetic materials are well suited to isolate WPT systems from conductive surfaces.
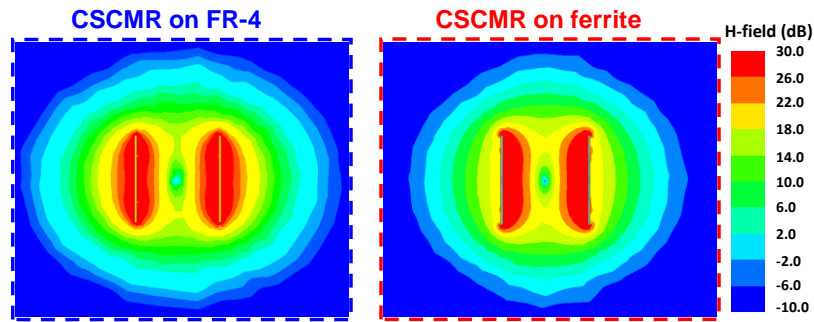
Figure 5.2. Magnetic field intensity of the CSCMR system in free space (a) with an FR-4 substrate, (b) with a ferrite substrate.

A.) CSCMR Performance on Body

The performance of our CSCMR system was studied on 26 unique locations of the human body, as shown in Figure 5.3 and Figure 5.4. The 26 locations were split into groups and categorized as either head (1-5), neck/bicep (6-10), arm (11-15), torso (16-21), and leg

44

(22-26). The torso category is the only group with 6 different locations due to its wide area of coverage compared to the other groups, which had 5 locations each. Our simulation setups were simplified to save computational resources by including for each case only the relevant part of the human body (instead of having the entire body model); thereby ignoring the other parts that have negligible effects on the performance of our WPT system.

The CSCMR systems used in this study operate in the ISM band at 27.12 MHz. Simulations were performed using ANSYS HFSS and the ANSYS human body model that includes the properties of the different human tissues [47]. Figure 5.4 shows the ANSYS human body model and the placement/orientation of the WPT system on the different locations. The measurements were conducted using a 3D printed support for the TX and RX, as shown in Figure 5.5, and for the following two spacings: a) flush against the body (i.e., 0 mm spacing), and b) 10 mm away from the body. The PTE, η, for each scenario, was measured using a Keysight Vector Network Analyzer (VNA). The PTE was defined as $\eta = |S_{12}|^2$.

Our simulated and measured results for all the placement locations on the human body (see Figure 5.3 and Figure 5.4) are shown in TABLE 5. I. The efficiencies of the CSCMR systems for all 5 placement categories (i.e., head, neck/bicep, torso, arm, and leg) were calculated by averaging the efficiency values of all locations under each category. The free-space case was included as a benchmark case to quantify the losses caused by the human body.
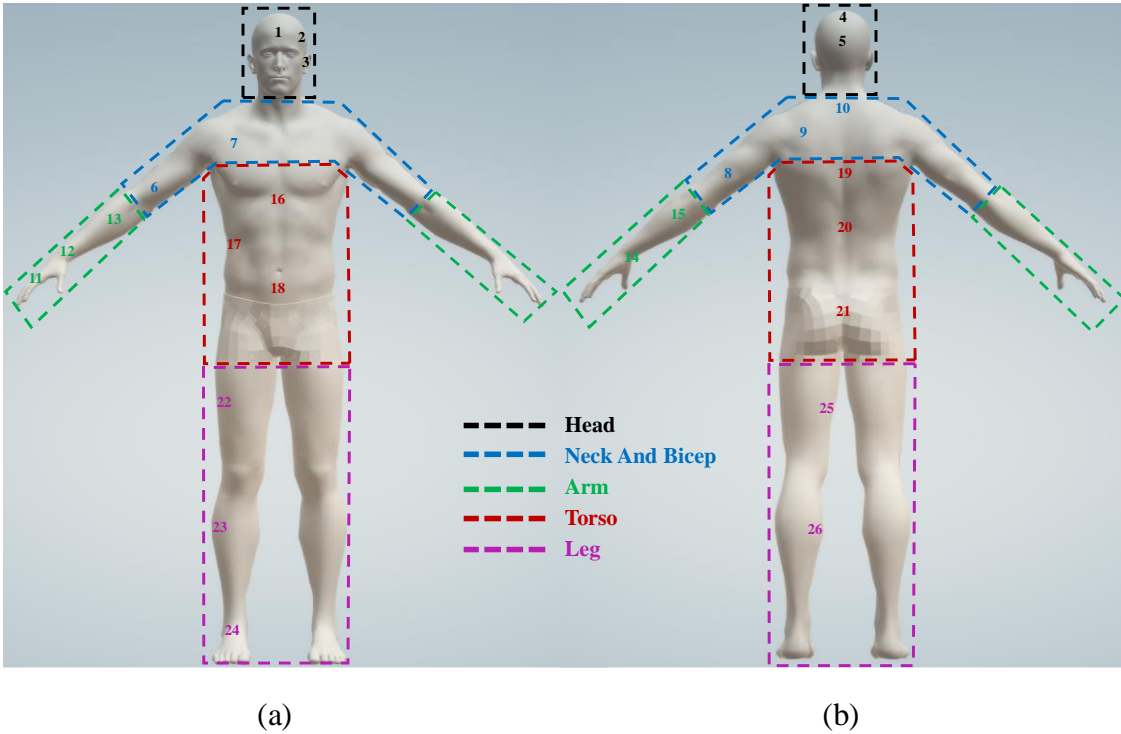
Figure 5.3. Human body model that outlines the 5 different groups of the CSCMR system's placement: (a) front view, (b) back view. [2]

Also, TABLE 5. I. shows the efficiency of the CSCMR systems for the locations that experienced the highest (upper back torso 19) and lowest (top of the wrist 12) amount of losses (i.e., efficiency drop). Measured results in TABLE5. I. show that for all the different placements on the body, the CSCMR system with the ferromagnetic substrate exhibits higher efficiency than the system with the FR- 4 substrates. Also, this can be illustrated by finding the average losses (i.e., each loss is calculated based on the difference between the reference case in free space and the case that is on the human body) using the 26 measurements at all placement locations on the human body. Specifically, the WPT system with the ferromagnetic substrate exhibited average losses of 1.6% and 0.6%, at a spacing of 0 mm and 10 mm, respectively. In contrast, the CSCMR with the FR-4 substrate exhibited losses of 7.2% and 3.0% at a spacing of 0 mm and 10 mm, respectively.
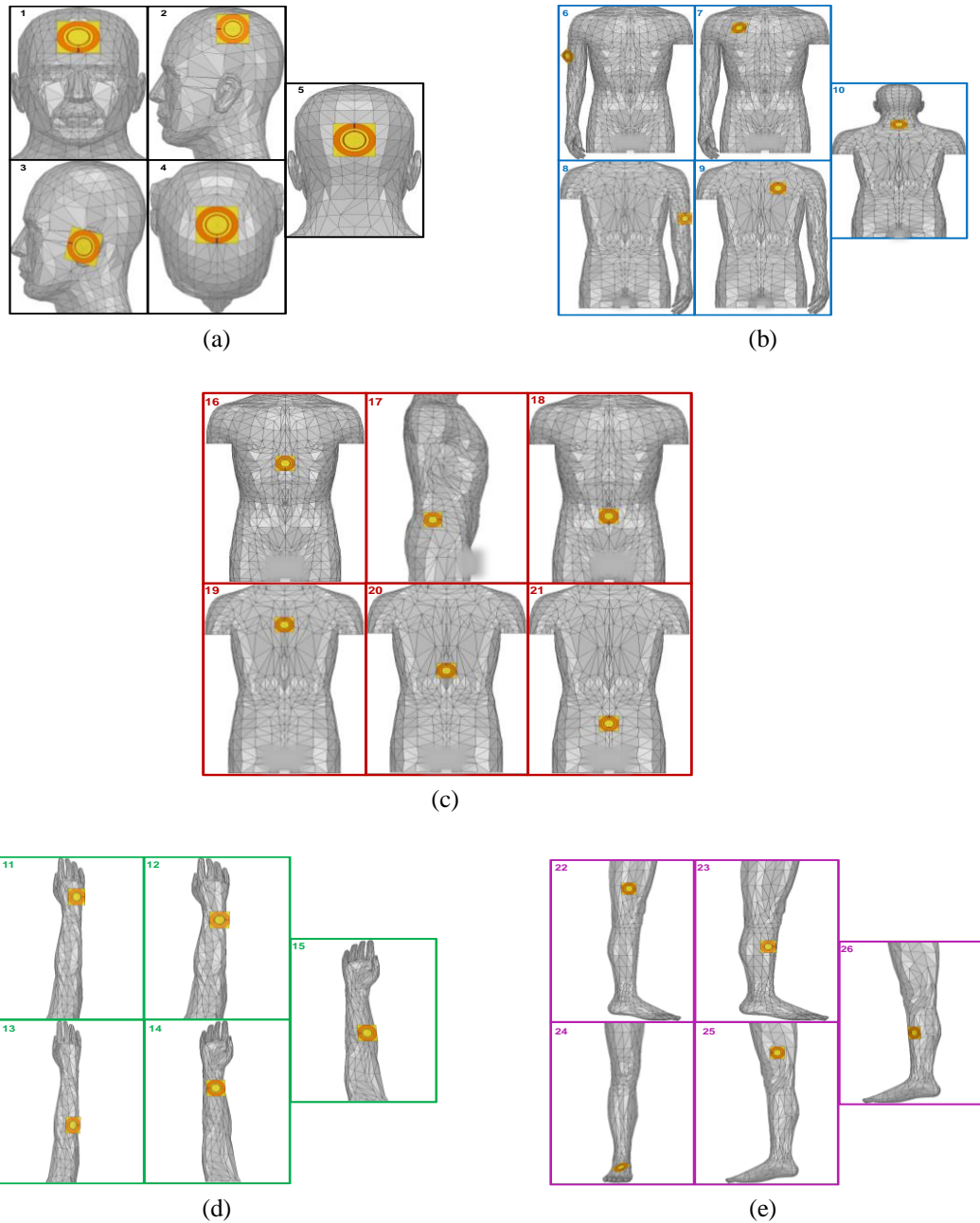
Figure 5.4. The ANSYS human body model [47] with the placement and orientation of the CSCMR system on 26 different locations: (a) head (1-5), (b) neck/bicep (6-10), (c) torso (16-21), (d) arm (11-15), and (e) leg (22-26).

TABLE 5. I.
PTE OF CSCMR SYSTEM ON THE HUMAN BODY.

Body Region	Power Transfer Efficiency (%)							
	CSCMR on FR-4				CSCMR on ferrite			
	Simulation		Measurements		Simulation		Measurements	
	0 mm	10 mm	0 mm	10 mm	0 mm	10 mm	0 mm	10 mm
Reference	73.43	73.43	70.0	69.9	75.27	75.27	71.0	70.2
Upper back torso (19)	65.56	69.70	60.1	66.2	71.90	73.52	69.0	70.4
Top of wrist (12)	71.77	73.20	64.6	68.0	74.96	75.25	69.0	69.6
Head	68.83	71.64	64.3	66.6	73.49	74.33	69.0	69.7
Neck/bicep	66.91	70.00	62.4	67.2	72.05	73.04	69.4	69.7
Torso	66.79	70.39	61.6	66.4	72.51	73.66	69.4	69.6
Arms	70.79	72.82	63.7	67.8	74.66	75.16	69.3	69.7
Legs	68.43	71.26	61.8	66.8	72.87	73.77	69.6	69.7

B.) Magnetic Field Distributions

The magnetic field intensities of our WPT system on a FR-4 substrate are compared here at the locations where they exhibited the highest and lowest simulated PTE in Figure 5.6. Specifically, the highest and lowest simulated PTEs occurred at the top of the wrist (see location 12 in Figure 5.3 and Figure 5.4) and the upper back of torso (see location 19 in Figure 5.3 and Figure 5.4), respectively. The field plots of Figure 5.6 justify why the simulated PTE achieves its highest and lowest values at these locations. This happens due to two reasons: (a) the upper torso is thicker and is wider area of the human body compared to the top of the wrist, which is also narrower than the size of our WPT TX and RX; therefore, higher WPT losses due to the properties of the human tissues occur at the upper torso location, and (b) the upper torso area has tissues with higher fat content than the wrist, which causes higher WPT losses at the upper torso. In fact, this conclusion and explanation are true for all of the placement locations, i.e., locations that are similar to the torso provided lower PTEs compared to locations similar to the top of the wrist (e.g., since the inner thigh region has a larger area than the WPT system and similar tissue composition to

that of the torso, it experiences similar losses). This is supported by the measured results

that are shown in TABLE 5. I.
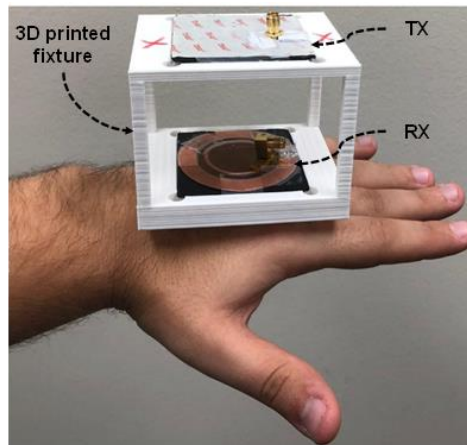
Figure 5.5. Magnetic field intensity of the CSCMR system in free space (a) with
an FR-4 substrate, (b) with a ferrite substrate.

(a)

(b)
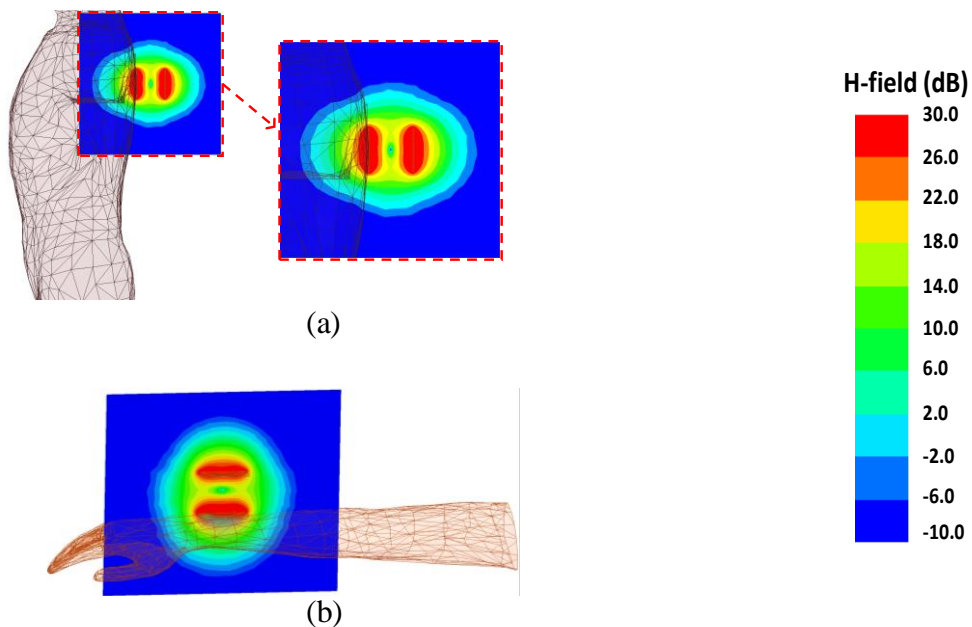
Figure 5.6. Magnetic field intensity of the CSCMR system with FR-4 substrate on
(a) the upper back of the torso and (b) top of the wrist.

In order to mitigate the losses experienced by our WPT system on the human body,

our CSCMR systems TX and RX are placed on a ferrite substrate instead of FR-4. Ferrites

are able to isolate the CSCMR elements from the influence of the human body because of

their high permeability. This high permeability confines the magnetic fields to the ferrite substrates, thereby not allowing them to reach and penetrate the human body. This reduces the intensity of the fields that interact with the human body, therefore diminishing the losses caused by the human body. The aforementioned statement is also supported by Figure 5.7, which compares the *H*-field distributions of the CSCMR systems with FR-4 and ferromagnetic substrates on the upper back of the torso. This figure clearly illustrates that when a ferrite substrate is used, the strongest field intensity (shown in red) does not spread towards the bottom of the TX and RX substrates; thus the strongest fields are confined between the TX and RX. Hence, as shown in Figure 5.7(a), when the WPT system on the FR-4 substrate is placed on the upper back of the torso, strong magnetic field intensities penetrate the substrate and reach the torso, thereby causing a decrease in PTE due to the losses occurring in the surrounding human tissues. On the contrary, the WPT system with the ferromagnetic substrate, as shown in Figure 5.7(b), confines the magnetic field in the area between the TX and RX, thus weakening the field intensities that reach the upper back torso, thereby reducing the losses caused by the surrounding human tissues and providing higher PTE than the WPT system on the FR-4 substrate.
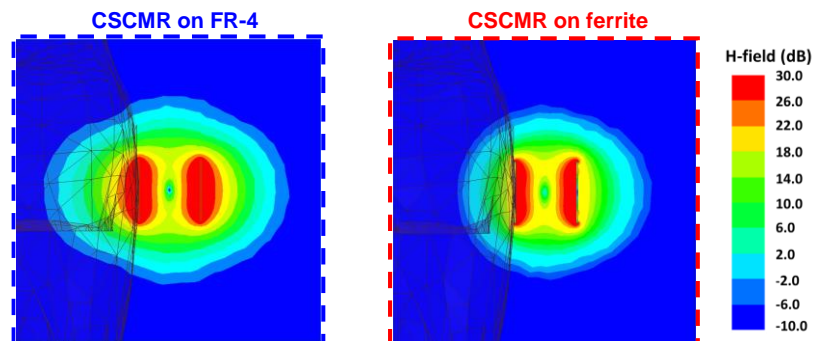
Figure 5.7. Magnetic field intensity of the CSCMR system on the upper back of the torso with (a) FR-4 substrate and (b) ferrite substrate.

C.) Specific Absorption Rate

Safety considerations are always of the utmost importance when designing WPT systems, and arguably SAR is one of the most important safety factors to consider. SAR is the measure of power absorbed per unit mass ($W\cdot kg^{-1}$) and has been the subject of extensive research efforts to ensure human safety. A high SAR may cause adverse effects on human health because biological tissues begin to absorb heat and exceedingly raise body core temperatures, especially within radio frequencies (RF). The standards on limiting RF exposure recognized by most RF engineers today are issued by the International Commission on Non-Ionizing Radiation Protection (ICNIRP 2020) [32] and the Institute of Electrical and Electronics Engineers (IEEE C95.1) [33]. According to the ICNIRP and IEEE guidelines, local SAR is measured as the power absorbed per 10-g of cubical mass. Peak-spatial SAR (psSAR) is defined as the maximum SAR and it should be studied for our WPT system that radiates in a small portion of the human body; therefore, local exposures are of greater importance (i.e., our system will always comply with the whole body-average SAR established guidelines). ICNIRP and IEEE imposes different guidelines to different areas of the human body, due to the temperature variations across the human body. The ICNIRP specifies the following body areas: (a) "Head and Torso" that consists of the head, eye, pinna, abdomen, back, thorax and pelvis, and (b) "Limbs" that consists of the upper arm, forearm, hand, thigh, leg and foot. The safety guidelines require that the psSAR within the head and torso areas remain less than 10 $W\cdot kg^{-1}$ and 2 $W\cdot kg^{-1}$ for occupational exposure (OE) and general public exposure (GPE) scenarios, respectively. For the limb's region, the psSAR should be less than 20 $W\cdot kg^{-1}$ and 4 $W\cdot kg^{-1}$ for OE and GPE scenarios, respectively.

Table 5. II. tabulates the maximum psSAR for each body region assuming an input power at the TX of 1 W over 10 grams of cubical mass, and the maximum possible input power in Watts based on the maximum psSAR. In our study, the head, neck/bicep, and torso body regions abide by the "Head and Torso" guidelines whereas the arms and legs abide by the "Limbs" guidelines. When the WPT system is placed flush to the skin (i.e., separation of 0 mm), the system with the ferrite substrate has a psSAR that, on average, is 2.5 times smaller than that corresponding psSAR of the system on FR 4. Also, compared to the case where the WPT system is placed flush to the skin, when there is a gap of 10 mm between the human body and the CSCMR systems, the average maximum psSAR for the body regions is 5 and 32 times smaller for the FR-4 and ferrite substrates, respectively. This is an important finding as it suggests that a gap between wearable WPT systems and the human body, as well as ferrite substrates, are crucial for maintaining psSAR within the ICINRP specifications, particularly for input power levels that are higher than 1 W.

TABLE 5. II.
MAXIMUM PSSAR OF CSCMR SYSTEMS ON THE HUMAN BODY AND MAXIMUM POSSIBLE INPUT POWER.

Body Region	Maximum psSAR ($W \cdot kg^{-1}$) in each body region				Maximum possible input power (W) for the maximum psSAR							
	CSCMR on FR-4		CSCMR on ferrite		CSCMR on FR-4				CSCMR on ferrite			
	0 mm	10 mm	0 mm	10 mm	0 mm		10 mm		0 mm		10 mm	
					GPE	OE	GPE	OE	GPE	OE	GPE	OE
HEAD	.7270	.1497	.4713	.0153	2.751	13.76	13.36	66.80	4.244	21.22	130.7	653.6
NECK/BICEP	.4730	.0844	.1260	.0113	4.230	21.14	23.70	118.5	15.87	79.37	177.0	885.9
TORSO	.5541	.1371	.2223	.0274	3.610	18.03	14.59	72.94	9.000	44.99	73.00	364.9
ARMS	.3025	.0662	.0932	.0108	13.22	66.12	60.42	302.1	42.92	214.6	370.4	1851
LEGS	.5313	.0736	.4357	.0164	7.530	37.64	54.35	271.7	9.181	45.90	243.9	1219

In Figures 5.8(a) and 5.8(b), the SAR distributions are shown for the CSCMR system with a FR-4 substrate on the forehead (see location 1 in Figure 5.3 and Figure 5.4) and on the top of the wrist (see location 12 in Figure 5.3 and Figure 5.4), respectively.

Notably, for an input power of 1 W, the simulated SAR on the forehead (which is the highest recorded from all body locations): (a) does not meet the ICNIRP specifications for general public exposure regardless of the choice of substrate, and (b) does meet the ICNIRP specifications for occupational exposures.

However, at the forehead location and assuming occupational exposures, our WPT systems on FR-4 and ferrite substrates meet the ICNIRP specifications as long as the input power does not exceed 1.38 W and 2.12 W, respectively. Likewise, Figures 5.8(c) and 5.8(d), show the SAR distributions for the CSCMR system with the ferrite substrate at the same locations. According to our results, to meet the SAR ICNIRP guidelines for general public exposure at the wrist location, the maximum input powers of the WPT systems on FR-4 and ferrite substrates are 1.87 W and 8.33 W, respectively.
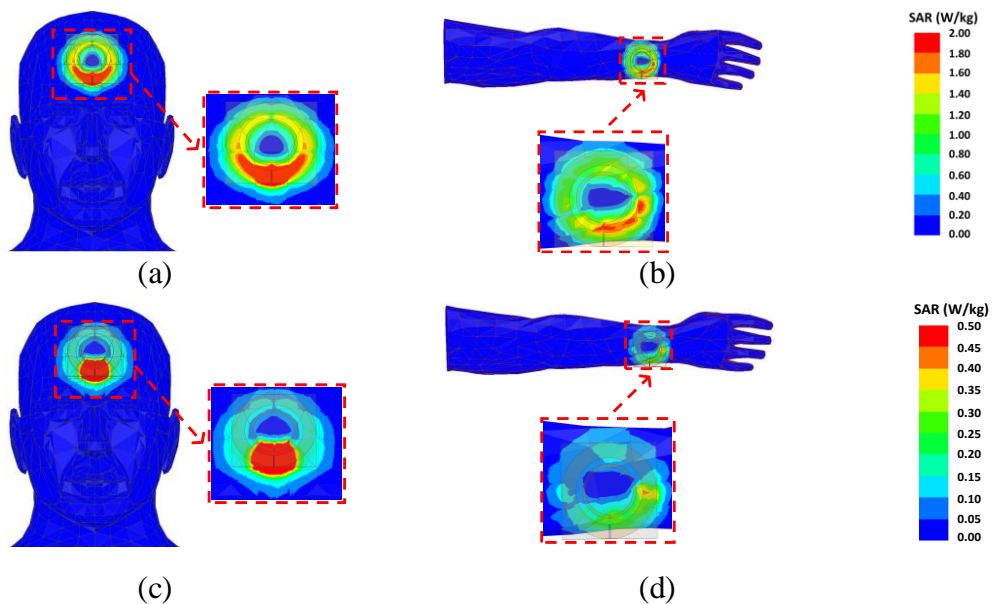
Figure 5.8. Simulated SAR of the CSCMR system: (a) with a FR-4 substrate on the forehead, (b) with a FR-4 substrate on the top of the wrist, (c) with a ferrite substrate on the forehead, and (d) with a ferrite substrate on the top of the wrist.

For occupational exposures of the WPT systems on FR-4 and ferrite substrates, the maximum input power levels increase to 4.80 W and 21.39 W, respectively. These higher input power levels are justified since: (a) the SAR is significantly smaller on top of the wrist compared to other locations (lowest recorded of all body locations), and (b) the SAR ICNIRP limits are higher for the limbs.

5.2   Simulation of Implantable Systems using SIM4LIFE

In this section, the effects of the human body on the Power Transfer Efficiency (PTE) of CSCMR WPT systems for wearable and implantable applications are studied using EM SIM4LIFE [50] software. Specifically, three placements are considered: 1) on top of the head (for neural implants), 2) the bottom of the back (for spinal cord stimulators), and 3) on top of the chest (for pacemakers). All simulations were done using the human model offered by SIM4LIFE known as Duke [51].

Here, the traditional CSCMR system as seen in Figure 3.1 is utilized for the design of the WPT system. The simulation of such systems is done with the EM SIM4LIFE software which utilizes a Finite-Difference Time-Domain (FDTD) EM solver. Also, SIM4LIFE is often used to simulate biological and anatomical environments since it offers highly accurate models of the human body, ranging from different genders to different ages. Our studies are conducted using the SIM4LIFE Duke model. Duke is based on a 34-year-old man of 1.77 m in height, weight of 70.2 kg, and his BMI is 22.4 kg/m^2 [21] and is shown in Figure 5.9. In this study, the areas of interest are the brain (the head), the heart (the chest) and the pelvic girdle (lower back), as shown in Figure 5.9. To simplify the mesh and speed-up the calculations, our loops were simulated as PEC since our main purpose is

54

to compare the efficiency of wearable and implantable CSCMR systems to the efficiency of the same systems in free space.
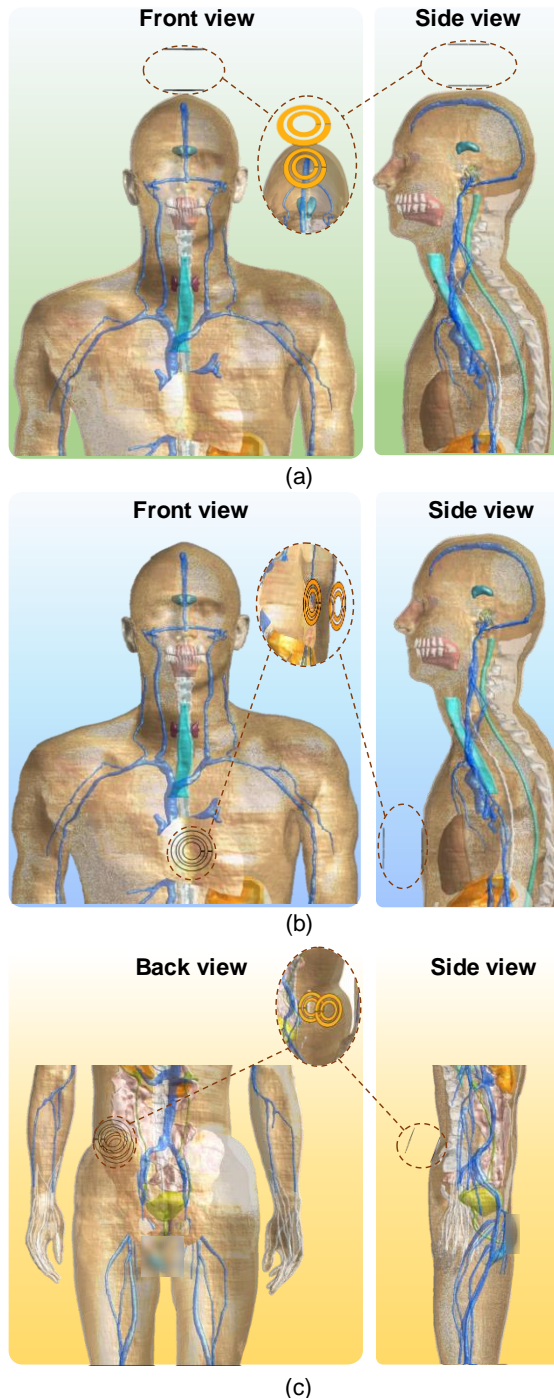
Figure 5.9. Duke human body model with CSCMR system on (a) top of the head (b) flush against his chest and (c) lower back.

In Figure 5.10, the PTE of a CSCMR system is calculated for the following positions: (a) top of the head, (b) chest (near heart area), and (c) lower back. In each scenario, the CSCMR design has a transfer distance of 60 mm, with geometrical parameters of $r_{TX} = 30$ mm, $r_S = 19$ mm, $W_{TX} = 7$ mm and $W_S = 6$ mm. The CSCMR design was placed 4 mm away from the top point of Duke's head, as shown in Figure 5.10(a). Furthermore, the CSCMR design was placed flush on Duke's chest, as shown in Figure 5.10(b). Finally, the CSCMR design was placed on Duke's lower back at an angle to best align the system against the body's arched area, as shown in Figure 5.10(c).

The traditional CSCMR design is given by each of the blue lines in Figure 5.10 and achieves nearly 100% efficiency at 40 MHz. This high PTE is due to the fact that the CSCMR system is modeled as a perfect electric conductor (PEC) instead of copper, thereby mitigating most of the losses due to resistance (which accounts for most of the losses in a simulation environment). The PTEs of the CSCMR systems on top of the head, the chest, and the lower back are 91.89%, 70.91%, and 86.19%, respectively. The resonant frequency and maximum efficiency are summarized in Table 5. III. The smallest drop of efficiency compared to the efficiency of the CSCMR system in free space occurred for the CSCMR system on top of the head. This is due to the 4 mm spacing and the fact that the region of the head is relatively sharp, therefore the human body has minimal effect on the CSCMR system in this case (approximately 8% drop in PTE occurs). The worst scenario occurs for the lower back scenario, shown in Figure 5.10(c), where the CSCMR system's PTE drops significantly down to 70.91%. This is justified because the dielectric properties of the human body create a mismatch in the RX, thereby shifting the resonant frequency. Therefore, a different lumped capacitance to achieve maximum Q-factor is required.
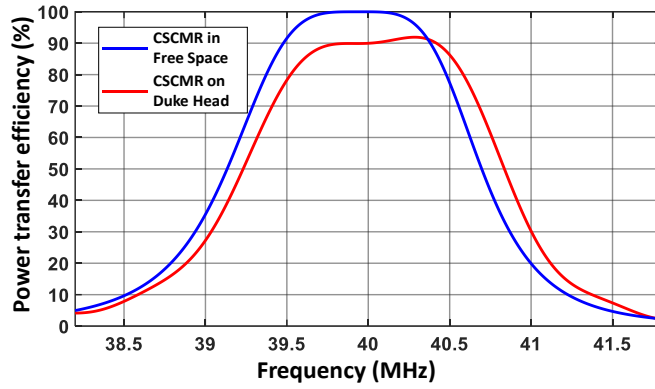
(a)
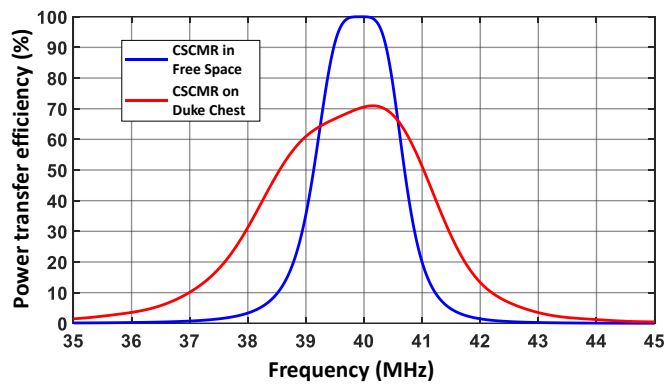
(b)
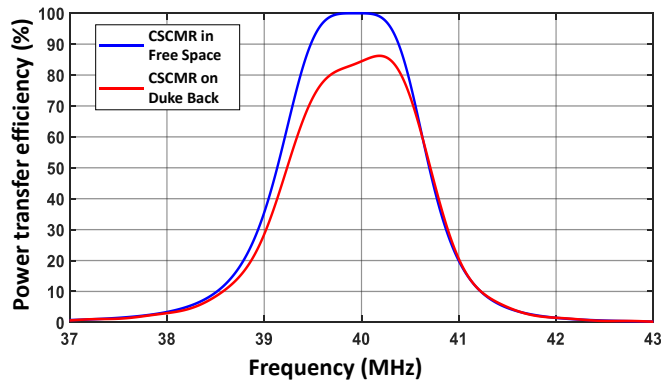
(c)

Figure 5.10. Simulated PTEs of CSCMR systems on Duke's (a) head, (b) chest and (c) lower back

TABLE 5. III. Performance of Wearable CSCMR Systems

	Frequency (MHz)	*Efficiency (%)*
Free space	40.00	99.98
Head	40.30	91.88
Chest	40.19	70.91
Lower back	40.20	86.19

Also, the performance of the implantable CSCMR system is examined here and it is shown in Figure 5.11. The new CSCMR design is designed for an implantable pacemaker. The system's geometry is a square of dimensions (r_S = 15 mm, W_S = 0.5 mm, r_{TX} = 14 mm, W_{TX} = 2 mm) that are well suited to the dimensions of the average pacemaker (in most cases larger than 40 mm by 40 mm). The proposed CSCMR system was encapsulated within the center of a 31 mm × 31 mm × 1 mm FR4 material for better isolation from the human body, thereby preventing a huge drop in the PTE (due to the human body material properties). The simulated efficiency is shown in Figure 5.12 for two implantation depths, namely, 10 mm and 20 mm. In free space, the new CSCMR design attains near 100% efficiency at a transfer distance of 10 mm. The 10 mm distance is appropriate for an implantable pacemaker, as the implantation depth of such devices is typically in the range of 5 mm to 20 mm. When the WPT system is implanted within Duke's chest as seen in Figure 5.11, at depths of 10 mm and 20 mm, the peak efficiency decreases by 7.37% and 52.25%, respectively, as summarized in Table 5. IV.
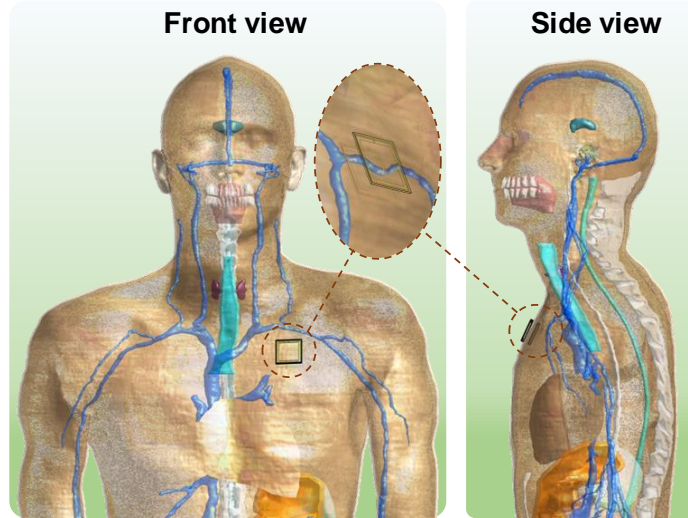
Figure 5.11. CSCMR systems implanted near Duke's chest to mimic the location of a pacemaker device
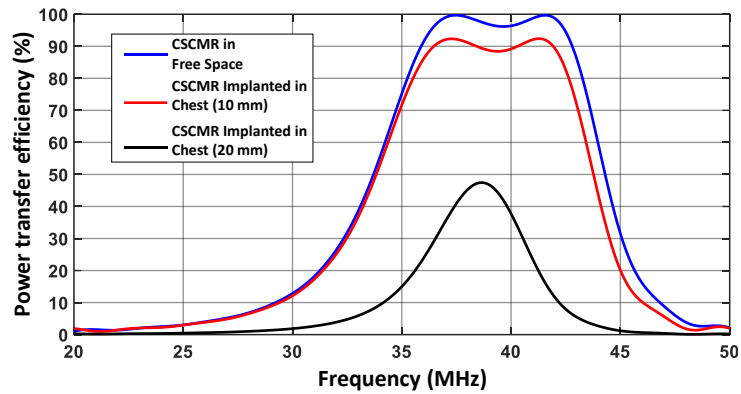
Figure 5.12. Simulated PTEs of CSCMR systems at various implantation depths

TABLE 5. IV. PERFORMANCE OF IMPLANTABLE CSCMR SYSTEMS

	Frequency (MHz)	*Efficiency (%)*
Free space	37.44	99.70
Chest (10 mm)	37.29	92.33
Chest (20 mm)	38.65	47.45

5.3)   Conclusion

In this research, the performance of CSCMR WPT systems was thoroughly studied for wearable and implantable applications. To the best of our knowledge, a rigorous study

such as the one presented here (which includes simulations and measurements for locations that cover the entire human body, also including the head, neck/bicep, torso, arms, and legs) has not been presented before; even though previous research has examined WPT wearable systems. The results demonstrate that when the WPT system is placed on the human body, its efficiency drops. The amount of this drop strongly depends on the particular placement location on the human body since the tissues near the WPT system absorb a portion of the generated EM fields. It is also shown that the drop of the WPT efficiency could be significantly reduced by placing the TX and RX WPT elements on ferromagnetic substrates instead of FR-4. Furthermore, our SAR study showed that to comply with ICNIRP RF exposure limits, CSCMR WPT systems should be placed at least 10 mm away from the human body and use a ferrite substrate for their RX element to lessen the intensity of EM fields that penetrate into human tissues.

CHAPTER VI. CONCLUSION

In this thesis, WPT systems were enhanced in numerous aspects. Specifically, the research in this thesis focused on the CSCMR method, which will almost certainly become a widely used method in years to come due to its great advantages over other WPT methods. Our research results illustrate that CSCMR systems with miniaturized size, extended range and safe operation in wearable and implantable systems can be developed. While there are numerous improvements that are still necessary before this technology is viable for everyday usage, the enhancements of CSCMR systems in this thesis could lead to the development of such systems.

References

[1] X. Wei, Z. Wang and H. Dai, "A Critical Review of Wireless Power Transfer via Strongly Coupled Magnetic Resonances," *Energies,* vol. 7, no. 7, pp. 4316-4341, Jul. 2014.

[2] [Online]. Available: https://www.turbosquid.com/3d-models/male-character-realistic-hair-3d-max/1080925.

[3] Market Research Future, "Global Wireless Power Transmission Market Research Report- Forecast 2022," Market Research Future, New York, 2016.

[4] J. Shin, S. Shin, Y. Kim, S. Ahn, S. Lee, G. Jung and S. Jeon, "Design and implementation of Shaped Magnetic Resonance Based Wireless power transfer system for Roadway Powered Moving electric vehicles," *IEEE Trans. Ind. Electron.,* vol. 61, no. 3, Mar. 2014.

[5] J. Lee and B. Han, "A Bidirectional Wireless Power Transfer EV Charger Using Self-Resonant PWM," *IEEE Trans. Power Electron.,* vol. 30, no. 4, pp. 1784-1787, Apr. 2015.

[6] D. Ahn and S. Hong, "Wireless Power Transmission With Self-Regulated Output Voltage for Biomedical Implant," *IEEE Trans. Ind. Electron.,* vol. 61, no. 5, pp. 2225-2235, May 2014.

[7] K. Chang-Gyun, S. Dong-Hyun, Y. Jung-Sik, P. Jong-Hu and B. H. Cho, "Design of a contactless battery charger for cellular phone," *IEEE Trans. Ind. Electron,* vol. 48, no. 6, pp. 1238-1247, Dec. 2001.

[8] M. Lu, M. Bagheri, A. P. James and T. Phung, "Wireless Charging Techniques for UAVs: A Review, Reconceptualization, and Extension," *IEEE Access,* vol. 6, pp. 29865-29884, 2018.

[9] J. Chen, R. Ghannam, M. Imran and H. Heidari, "Wireless Power Transfer for 3D Printed Unmanned Aerial Vehicle (UAV) Systems," in *IEEE Asia Pacific Conference on Postgraduate Research in Microelectronics and Electronics (PrimeAsia)*, Chengdu, 2008.

[10] W. Na, J. Park, C. Lee, K. Park, J. Kim and S. Cho, "Energy-Efficient Mobile Charging for Wireless Power Transfer in Internet of Things Networks," *IEEE Internet of Things Journal,* vol. 5, no. 1, pp. 79-92, Feb. 2018.

[11] P. V. Nikitin, K. V. S. Rao and S. Lazar, "An Overview of Near Field UHF RFID," *IEEE Int. Conf.,* pp. 167-174, Mar. 2007.

[12] K. Finkenzeller, "RFID Handbook: Fundamentals and Applications in Contactless Smart Cards and Identification," New York, Wiley, 2003, pp. 65-112.

[13] N. Tesla, Proc. Thirteenth Anniversary Number of the Electrical World & Engineer, 1904.

[14] S. Y. R. Hui, W. Zhong and C. K. Lee, "A Critical Review of Recent Progress in Mid-Range Wireless Power Transfer," *IEEE Transactions on Power Electronics,* vol. 29, no. 9, pp. 4500-4511, 2014.

[15] A. Kurs, A. Karalis, R. Moffatt, J. Joannopoulos, P. Fisher and M. Soljacic, "Wireless Power Transfer via Strongly Coupled Magnetic Resonances," *Science,* vol. 317, no. 5834, pp. 83-86, July 2007.

[16] A. W. Green and J. T. Boys, "10 kHz inductively coupled power transfer-concept and control," in *ICPE-VSD*, 1994.

[17] J. T. Boys, G. A. Covic and A. W. Green, "Stability and control of inductively coupled power transfer systems," *Proc. Electric Power Appl.,* vol. 147, no. 1, pp. 37-43, 2000.

[18] G. A. J. Elliott, G. A. Covic, D. Kacprzak and J. T. Boys, "A new concept: Asymmetrical pick-ups for inductively coupled power transfer monorail systems," *IEEE Trans. Magn.,* vol. 42, no. 10, pp. 3389-3391, 2006.

[19] B. Choi, J. Nho, H. Cha, T. Ahn and S. Choi, "Design and implementation of low-profile contactless battery charger using planar printed circuit board windings as energy transfer device," *IEEE Transactions on Industrial Electronics,* vol. 51, no. 1, pp. 140-147, 2004.

[20] "Wireless Power Consortium Website," 2013. [Online]. Available: https://www.wirelesspowerconsortium.com/.

[21] F. S. Sandoval, S. M. T. Delgado, A. Moazenzadeh and U. Wallrabe, "A 2-D Magnetoinductive Wave Device for Freer Wireless Power Transfer," *IEEE Transactions on Power Electronics,* vol. 34, no. 11, pp. 10433-10445, Nov. 2019.

[22] A. Kumar, S. Pervaiz, C.-K. Chang, S. Korhummel, Z. Popovic and K. Afridi, "Investigation of power transfer density enhancement in large air-gap capacitive wireless power transfer systems," in *IEEE Wireless Power Transfer Conference*, Boulder, 2015.

[23] [Online]. Available: http://web.mit.edu/viz/EM/visualizations/coursenotes/modules/inductance.pdf.

[24] Y. H. Sohn, B. H. Choi, E. S. Lee, G. C. Lim, G. Cho and C. T. Rim, "General Unified Analyses of Two-Capacitor Inductive Power Transfer Systems: Equivalence of Current-Source SS and SP Compensations," *IEEE Transactions on Power Electronics,* vol. 30, no. 1.

[25] D. Liu, "Novel Strongly Coupled Magnetic Resonance Systems," FIU Electronic Theses and Dissertations, Miami, 2018.

[26] O. Jonah, S. V. Georgakopoulos and M. M. Tentzeris, "Optimal Design Parameters for Wireless Power Transfer by Resonance Magnetic," *IEEE Antennas Wireless Propag. Lett.,* vol. 11, pp. 1390-1393, 2012.

[27] C. A. Balanis, Antenna Theory: Analysis and Design, New Jersey: Wiley, 2005.

[28] R. Lundin, "A handbook formula for the inductance of a single-layer circular coil," *Proc. IEEE,* vol. 73, no. 9, pp. 1428-1429, September 1985.

[29] D. Fang, Handbook of Electrical Calculations, Jinan: Shandong Sci. Technol. Press, 1994.

[30] J. L. Volakis, Antenna Engineering Handbook, New York: McGraw-Hill, 2007.

[31] A. K. RamRakhyani, S. Mirabbasi and C. Mu, "Design and optimization of resonance-based efficient wireless power delivery systems for biomedical implants," *IEEE Trans. Biomed. Circuits Syst.,* vol. 5, no. 1, pp. 48-63, Feb. 2011.

[32] H. Hu and S. V. Georgakopoulos, "Multiband and Broadband Wireless Power Transfer Systems Using the Conformal Strongly Coupled Magnetic Resonance Method," *IEEE Transactions on Industrial Electronics,* vol. 64, no. 5, pp. 3595-3607, 2017.

[33] K. Bao, C. L. Zekios and S. V. Georgakopoulos, "Miniaturization of SCMR Systems Using Multilayer Resonators," *IEEE Access,* vol. 7, pp. 143445-143453, 2019.

[34] X.Yu, T. Skauli, B. Skauli, S. Sandhu, P. B. Catrysse and S. Fan, "Wireless power transfer in the presence of metallic plates: Experimental results," in *AIP Adv.*, 2013.

[35] W. Zhong, C. K. Lee and S. Y. R. Hui, "General Analysis on the Use of Tesla's Resonators in Domino Forms for Wireless Power Transfer," *IEEE Transactions on Industrial Electronics,* vol. 60, no. 1, pp. 261-270, Jan. 2013.

[36] X. Zhang, S. L. Ho and W. N. Fu, "Quantitative Design and Analysis of Relay Resonators in Wireless Power Transfer System," *IEEE Transactions on Magnetics,* vol. 48, no. 11, pp. 4026-4029, Nov. 2012.

[37] Z. Ye, X. D. Y. Sun, C. Tang, Z. Wang and Y. Su, "Energy Efficiency Analysis of U-Coil Wireless Power Transfer System," *IEEE Transactions on Power Electronics,* vol. 31, no. 7, pp. 4809-4817, July 2016.

[38] Z. Ye, P. Wang, L. Hu and W. Zhu, "Ladder-Type Mid-Range Wireless Power Transfer," in *IEEE PELS Workshop on Emerging Technologies: Wireless Power Transfer (Wow)*, Montréal, QC, 2018.

[39] E. I. Green, "The story of Q" Bell Telephone System-Technical Publication Monograph 2491," *Amer. Scientist,* vol. 43, pp. 1-11, Oct. 1955.

[40] M. Kiani, U. Jow and M. Ghovanloo, "Design and Optimization of a 3-Coil Inductive Link for Efficient Wireless Power Transmission," *IEEE Transactions on Biomedical Circuits and Systems,* vol. 5, no. 6, pp. 579-591, Dec. 2011.

[41] C. Akyel, S. Babic and S. Kincic, "New and fast procedures for calculating the mutual inductance of coaxial circular coils (circular coil-disk coil)," *IEEE Transactions on Magnetics,* vol. 38, no. 5, pp. 2367-2369, Sept. 2002.

[42] D. Ahn and S. Hong, "A Study on Magnetic Field Repeater in Wireless Power Transfer," *IEEE Transactions on Industrial Electronics,* vol. 60, no. 1, pp. 360-371, Jan. 2013.

[43] C. A. Balanis, Advanced Engineering electromagnetics, Hoboken, NJ: John Wiley & Sons, 2012.

[44] M. Soma, D. C. Galbraith and R. L. White, "Radio-Frequency Coils in Implantable Devices: Misalignment Analysis and Design Procedure," *IEEE Transactions on Biomedical Engineering,* Vols. BME-34, no. 4, pp. 276-282, April 1987.

[45] W. T. Joines, Y. Zhang, C. Li and R. L. Jirtle, "The measured electrical properties of normal and malignant human tissues from 50 to 900 MHz," *Medical Physics,* vol. 21, no. 4, pp. 547-550, April 1994.

[46] [Online]. Available: https://www.fair-rite.com/flexible-ferrite/.

[47] ANSYS Inc., "Electromagnetic Safety in Wireless Communications and Bio-Medical Technologies," ANSYS white paper, 2014.

[48] "ICNIRP Guidelines for Limiting Exposure to Time-Varying Electric and Magnetic Fields (100 kHz-300GHz)," *Health Phys.,* vol. 118, pp. 483-524, March 2020.

[49] IEEE, C95.1-2019, "IEEE Standard for Safety Levels With Respect to Human Exposure to Electric, Magnetic, and Electromagnetic Fields, 0 Hz to 300 GHz," IEEE, Oct. 2019.

[50] [Online]. Available: https://zmt.swiss/sim4life/.

[51] G. M. C, N. E, M. H, H. E, F. S, G. L, J. M, H. I, D. G. F, L. B, C. E, S. D, K. W and K. N, "Development of a new generation of high-resolution anatomical models for medical device evaluation: the Virtual Population 3.0," *Physics in Medicine and Biology,* pp. 5287-5303, 2014.

[53] U. Jow and M. Ghovanloo, "Design and Optimization of Printed Spiral Coils for Efficient Transcutaneous Inductive Power Transmission," *IEEE Transactions on Biomedical Circuits and Systems,* vol. 1, no. 3, pp. 193-202, Sept. 2007.